Journal of Ocean Engineering and Marine Energy
https://doi.org/10.1007/s40722-024-00351-z

RESEARCH

Exploring submergence impact on flow-induced motion energy-harvesting with circular-triangular prisms

Ali Sharifi[1] · **Mohammad Omidyeganeh**[2] · **Mehran Masdari**[2]

Received: 8 August 2024 / Accepted: 26 September 2024

Abstract

Recent advancements in energy-harvesting have utilized Flow-Induced Motion (FIM) as a renewable source, diverging from past efforts aimed at minimizing FIM's adverse effects. This study introduces kinetic energy converters using alternating lift technology (ALT), employing a prism with a Circular-Triangular (Cir-Tria) shape, coupled with a spring and damper, to generate energy. Utilizing computational fluid dynamics in OpenFOAM for Reynolds numbers between 2×103 and 13×103 and varying submergence depth ratio from 0.98 to 5.91, this research employs a moving computational grid, two-dimensional incompressible Navier–Stokes equations, the k-omega Shear Stress Transport (SST) turbulence model, the Volume of Fluid, VOF, two-phase model, and the cylinder mass–spring–damper equation. Findings show that approaching the flow surface negatively impacts the FIM response due to the interaction of vortices from the flow surface and the prism's upper shear layer. This interaction weakens and neutralizes the upper vortices, altering the flow structure around the prism and the governing FIM phenomena. Proximity to the free surface significantly affects FIM responses, with a notable decrease in vibration amplitude and energy conversion as the submergence depth ratio increases from 0.98 to 5.91. Maximum system efficiency of 1.4% is observed in the VIV initial branch at infinite submergence (single-phase flow). Beyond a submergence depth ratio of 5.91, FIM amplitude and energy conversion flatten, indicating negligible free surface effects.

Keywords Energy-harvesting · Submergence depth · Cir-Tria prism · Flow-induced motion (FIM)

List of Symbols

U	Flow velocity
L	Length of cylinder
K	Spring stiffness
M	Total mass of VIV system
D	Diameter of the cylinder
C_{total}	System damping coefficient
$F_{\text{fluid}.y}(t)$	Total fluid force
ρ	Water density
υ	Kinematic viscosity
$\text{Re} = UD/\nu$	Reynolds number
T_{osc}	Period of oscillation
A	Amplitude of oscillation
$A^* = A/D$	Amplitude ratio
$A_{\max}$	Maximum Amplitude of oscillation
S	Submergence depth
$S^* = S/D$	Submergence depth ratio
$m^* = M/m_{\text{disp}}$	Mass ratio
m_{add}	Added mass
f_{osc}	Oscillating cylinder frequency
$f_{n.\text{water}} = \left(\frac{1}{2\pi}\right)\sqrt{\frac{K}{M+m_{\text{add}}}}$	Cylinder's natural frequency
$f^* = \frac{f_{\text{osc}}}{f_{n.\text{water}}}$	Frequency ratio
$U^* = \frac{U}{f_{n.\text{water}}D}$	Reduced velocity

✉ Mehran Masdari
mehran.masdari@city.ac.uk

[1] Faculty of New Sciences and Technologies, University of Tehran, Tehran, Iran

[2] School of Science and Technology, City University of London, London, UK

1 Introduction

As a result of the recent development of renewable energy conversion technologies, various energy converters have been manufactured to harvest renewable energy. The flow-induced motion (FIM) phenomenon has also been used for

Published online: 14 October 2024

energy containment from low-velocity ocean and river currents (Rostami and Armandei 2017). When a bluff body is mounted with flexibility or has ductility, it oscillates because of fluctuating forces caused by vortex shedding. FIM changes the creation and release of vortices. Fluid–structure interaction (FSI) causes distinct behaviors in the bluff body, specifically Vortex-Induced Vibration (VIV) and galloping, together with their interactions during the transition from VIV to galloping. These phenomena are known for their non-linear traits and unique behaviors. VIV and galloping are categorized into distinct branches of vibration created by vortices, with their amplitude and frequency influenced by the velocity of fluid flow (Zhang et al. 2017, 2018). In some machinery and mechanical problems where the fluid flow passes over the bluff body, the induced current movement is known as a destructive phenomenon since it causes damage caused by fatigue. Therefore, a lot of effort has been made to restrain this phenomenon, and the research has been done, focused on reducing the effects of the induced current movement. (Bernitsas et al. 2008) introduced the VIVACE (Vortex-Induced Vibration for Aquatic Clean Energy) converter, utilizing Alternating Lift Technology (ALT) to harness energy from low-speed flows by addressing the FIM phenomenon. Research on FIM energy converter has been done by Lee et al. (2011), Sun et al. (2017) and Park et al. (2013) using laboratory methods and Ding et al. (2016) using numerical methods. These resources provide researchers with precise information about VIV and galloping and their interaction, which facilitates research in this field of FIM.

Khalak and Williamson (1996) and Zhao et al. (2013) have extensively studied the circular and square cylinder FIM responses. They introduced three different VIV branches (initial branch, upper branch, and lower branch) and galloping based on the amplitude and oscillation frequency according to the fluid flow velocity. Bernitsas (2016) and Kim and Bernitsas (2016) also reached similar conclusions about FIM branches. In 2011, the simulated spring–damper system with a controller (Lee et al. 2011) was implemented by introducing a controller to adjust the K values. An experimental and systematic study of the VIVACE converter's restrained hydrokinetic power performance (within and in a low-turbulence free surface water channel) has been carried out in the Marine Renewable Energy Laboratory (MRE-Lab) of the University of Michigan. In this study, the amplitude and the spectrum of K changes are around 400N/m < K < 1800 N/m and it is set by the computerized controller after comprehensive calibration. The results illustrated that the peak observed amplitude is equal to 1.78D at the stiffness of $K =$ 1200 N/m, and also the amplitude synchronization changes decrease as the velocity decreases since the increase in the spring stiffness increases its restoring force (which is applied to the cylinder), and this results in the VIV synchronization range moving at a higher flow rate. Moreover, numerical studies based on different CFD methods have been done to study the FIM responses. (Zhang et al. 2018) studied the rectangular cylinder FIM responses using Fluent. (Ding et al. 2016) analyzed the FIM responses of non-circular cross-sectional cylinders via the CFD method based on OpenFOAM. (Zhao et al. 2015) studied two cylinders in a row and two cylinders side by side with a two-dimensional (2D) simulation. Similarly, (Mao and Zhao 2017) simulated the underwater connected rotating cylinder's FIM using Fluent software and then examined it using neural networks. The effect of FIM responses of a circular cylinder upstream on a flat plate with one degree of freedom downstream was investigated using numerical simulations in laminar flow (Jebelli and Masdari 2022a, b). In a similar way, the effect of a rotating cylinder placed on top of two parallel flat plates was studied (Babaie et al. 2022). Effect of adding rotational degree of freedom by giving centrifugal force to the rotating cylinder on vibration and rotational response as well as hydrokinetic energy conversion in Reynolds number $2 \times 10^3 < \mathrm{Re} < 13 \times 10^3$ were investigated.

Previous researches principally focused on FIM responses in deep water or single-phase flow. The submergence depth effects on FIM responses were largely ignored. However, it is necessary to investigate the submergence depth effects because the vortex pattern structure may change (Raghavan 2007). When the FIM energy converter is adjacent to the free surface, even if the FIM energy converter is entirely submerged, the submergence depth affects the FIM energy conversion. Until now, negligible studies have been conducted on the submergence depth effects. Reichl et al. (2005) conducted a series of numerical investigations of the flow through a fixed cylinder when the cylinder is close to the free surface. Zhu et al. (2000), Carberry et al. (2004) studied the free surface effects on FIM responses only for deterministic vibration. In Raghavan et al. research and similarly reported by Bernitsas, et al. (2007), Raghavan (2007), the FIM synchronization range is greatly reduced by decreasing the submergence depth. However, the aforementioned studies focused on FIM amplitude and frequency responses, not on energy conversion. Furthermore, the vortex patterns associated with the submergence depth are not known. The closest related research on the free surface effects or submergence depth is limited to the (Gu et al. 2020) studies. However, the aforementioned studies are focused on the FIM. The things mentioned above represent the need for research in the field of studying the submergence depth effects and disturbance caused by the free surface deformation, and improving the alternating lift technology converter performance in terms of efficiency and creating the least destructive effects is one of the research objectives.

In this research, a series of two-dimensional numerical simulations have been done to investigate the submergence

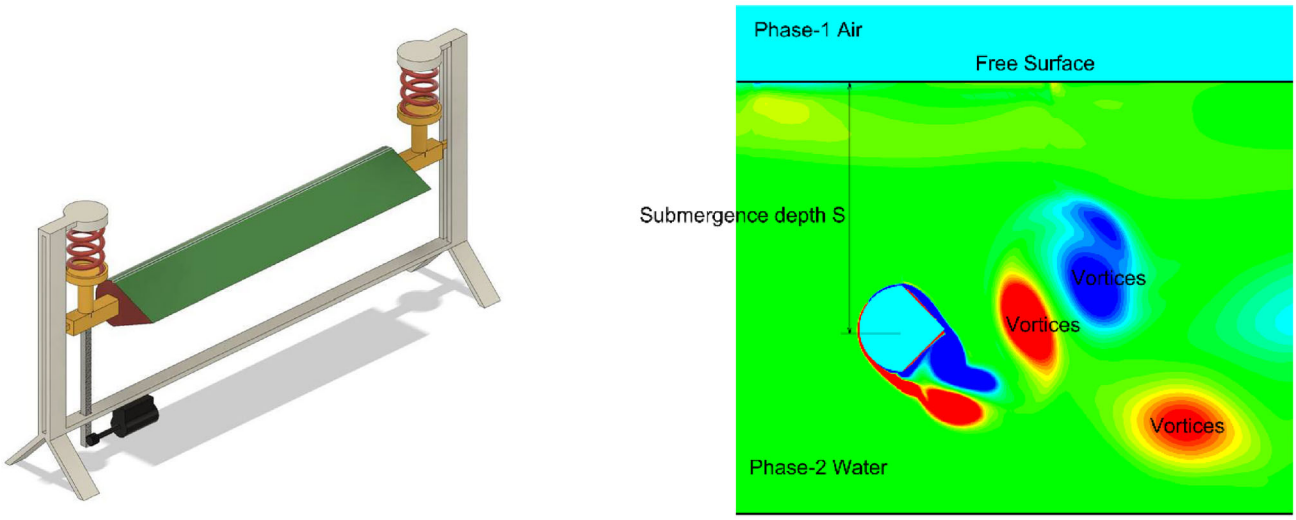

Fig. 1 **a** FIM hydrokinetic energy conversion system (**b**) and Simplified sketch near the free surface

depth effect on FIM energy conversion and to obtain the eligible depth. The FIM responses of a prism under different submergence depth ratios (0.98 to 5.91) have been studied. The study covers a range of reduced velocity from 2 to 14 ($2 \times 10^3 < \mathrm{Re} < 13 \times 10^3$), corresponding to the TrSL2 layer classification, as defined by (Zdravkovich 2003). Besides, to verify the numerical method, the CFD results have been compared with the experimental results again.

2 Problem description

Figure 1a depicts the FIM energy conversion system, which is represented as an elastically supported cylinder or prism according to reference (Gu et al. 2020). To enhance comprehension of this phenomenon, a simplified schematic is depicted in Fig. 1b. The cylinder is fully submerged and secured with linear bearings to allow for unrestricted oscillation. The Cir-Tria prism is parallel to both the bottom and the free surface. Additionally, it has been documented that the lateral amplitude in FIM exceeds the amplitude in the longitudinal direction, as per reference (Ding et al. 2015). Therefore, only the transverse reaction is analyzed in this study. S denotes the depth of submergence. It is the ratio of submergence depth. The damping refers to the entire system, which includes the generator, the transmission mechanisms, and the spring constant. Also, any mechanical slippage effects are neglected.

This work is based on towing tank tests conducted in the laboratory for Fluid–Structure Interaction (FIM) and computational simulation as reported by Gu et al. (2020). The FIM hydrokinetic energy converter causes free surface deformation when situated near the free surface, especially at low submergence depths. The submergence depth plays a crucial role and greatly impacts the FIM. Numerical approaches can be used to examine the FIM reactions and assess free surface deformation, which is challenging to capture in experiments.

Table 1 Physical model parameters

Description	Symbol	Value
Diameter of the cylinder	D (m)	0.0508
Spring stiffness	K (N/m)	43.5
Mass ratio	m^*	2.4
Velocity ratio	U^*	2–14
Natural frequency	$f_{n.\mathrm{water}}$(Hz)	0.4
Kinematic viscosity	$\nu(\mathrm{m}^2/\mathrm{s})$	1.14×10^{-6}
Water density	$\rho(\mathrm{kg}/\mathrm{m}^3)$	1000
Submergence depth ratio	S^*	0.98–5.91
Volume flow rate	Q	0.0021–0.0145

The design parameters illustrated in Table 1 are the same as the VIV system determined in the reference (Khalak and Williamson 1999). The major parameters are listed in Table 1. According to this table, the ratio of submergence depths ranges from 0.98 to 5.91 and the fluid flow rate varies from 0.04 m/s to 0.28 m/s ($2 \times 10^3 < \mathrm{Re} < 13 \times 13^3$).

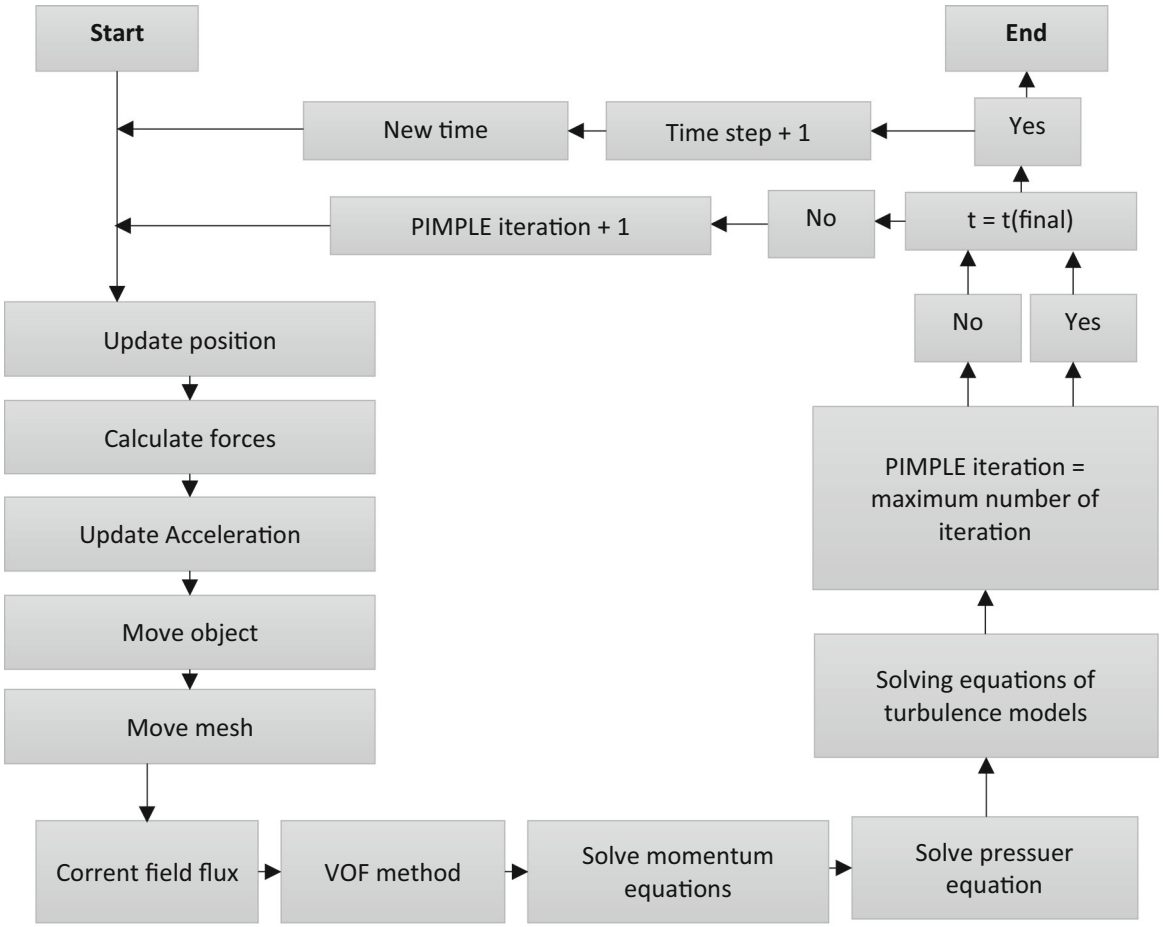

Fig. 2 Flowchart of the numerical simulation

3 Equation of motion

The equation of motion of the cylinder or prism attributable to FIM is represented as a mass–spring–damper equation, which is an ordinary, second-order, and linear equation (Bernitsas et al. 2006).

$$M\ddot{y} + C_{total}\dot{y} + Ky = F_{fluid.y}(t) \tag{1}$$

The total converted FIM power from the cylinder in one cycle is defined as the following equation:

$$P_{\mathrm{FIM}} = \frac{1}{T_{\mathrm{osc}}} \int_0^{T_{\mathrm{osc}}} F_{\mathrm{fluid}.y}(t)\dot{y}\mathrm{d}t. \tag{2}$$

The power equation for VIV of a cylinder can be simplified by incorporating the mass–spring–damper system. Assuming sinusoidal vibrations and substituting the relevant terms, the output power of the cylinder under VIV can be expressed as follows after mathematical simplification (Bernitsas et al. 2006):

$$P_{\mathrm{FIM}} = 8\pi^3 (M + m_{\mathrm{add}})\zeta_{\mathrm{total}} f_{n.\mathrm{whater}} A^2 f_{\mathrm{osc}}^2, \tag{3}$$

where the damping ratio is defined as Eq. (4):

$$\zeta_{\mathrm{total}} = \frac{C_{\mathrm{total}}}{2\sqrt{K(M + m_{\mathrm{add}})}}. \tag{4}$$

Nevertheless, the power in the fluid can be defined as the product of the kinetic pressure head and the fluid flow rate (pressure and flow rate are volumetric):

$$P_{\mathrm{fluid}} = PQ \tag{5}$$

$$Q = A_{\mathrm{flow}} U. \tag{6}$$

The cylinder depicted surface is on the contrary to flow, and based on the Bernoulli equation, the kinetic pressure head is as follows:

$$P = \frac{1}{2}\rho U^2. \tag{7}$$

Therefore, the fluid power equation is as follows:

$$P_{fluid} = \frac{1}{2}\rho U^3 L(D + 2A) \tag{8}$$

Moreover, the converter efficiency is the ratio of the generated power to the fluid power:

$$\eta_{\mathrm{FIM}} = \frac{P_{\mathrm{FIM}}}{P_{\mathrm{fluid}}}. \tag{9}$$

Eventually, the purpose of obtaining these equations is to calculate the extractive power and efficiency of the FIM system.

4 Numerical model

This research utilizes computational fluid dynamics with the OpenFOAM program for problem-solving. Figure 2 represents a complete flowchart of the computational steps of the InterFoam solver (a solver in the OpenFOAM software), which is used in this research. According to this flowchart, the motion solver (responsible for calculating forces, acceleration, cylinder motion, and the grid) is first applied, after which the new flux of the flow field is determined as a result. After this stage, respectively, the two-phase model is applied, then the momentum equations and the pressure equation, and finally, the turbulence model equations are solved. Besides, if the repetition number of an internal loop of the velocity—pressure coupling (pimple) ends, these calculations enter a new time step and this process will continue until the end of the time interval.

The volume of fluid (VOF) method used in this research implies the scaling function definition, which was submitted by Hirt and Nichols (1981) and has created a new direction in multi-phase flow simulation. This scale function represents the type of fluid or fluids that include the computational cells. InterFoam is a multi-phase solver in OpenFOAM, which is used to simulate the sharing surface of two immiscible fluids using the volume of fluid.

This research utilizes URANS turbulence models to solve equations for time-averaged values and turbulent oscillation flow. The instantaneous field is defined as the sum of average and fluctuating components. This simulation utilizes the K-Omega SST turbulence model.

The discretization method used for the mass–spring—damper equation is the Newmark-beta method, which is a kind of numerical integral method to solve a particular form of differential equations. This method has been named Newmark (1959), a former professor of civil engineering at the University of Illinois Urbana-Campaign, and finally, the Pimple couple (Oliveira and Issa 2001) used in this research is a pressure-based couple from the separated category, which is very similar to the piezo coupler. In the discrete algorithm, the governing equations are solved consecutively. In the discrete algorithm, the governing equations are solved sequentially. In contrast, the coupled method solves the equations simultaneously. In the pressure-based approach, the velocity field is obtained from the motion and pressure equations by solving Poisson's equation.

4.1 Computational domain

The computational grid and domain as well as the boundary conditions are represented in Figs. 3 and 4, in which the domain length and width are set to 50D and 30D, and the subdomain diameter is set to 5D, D is the prism diameter. Variable parameters in this research tests are submergence depth (S) and flow velocity (U). Figure 3 shows a two-phase flow in the input boundary range with air as phase one and water as phase two. The grid in the free surface region, as depicted in Fig. 4, is significantly decreased to see the free-surface impacts on the oscillation induced by the vortex. The computing grid used here is an organized square grid. The mentioned grid is a type of movable grid with a morphing mesh technique, and the grid moves along with it on the prism solid boundaries, in this way, the interaction between the structural component and the fluid is conscientiously tracked.

4.2 Numerical method validation

The computational model convergence was verified by comparing the CFD findings with the laboratory data for the circular cylinder in terms of amplitude ratio and frequency ratio. The major characteristics of the VIV system for the circular cylinder were established based on earlier tests (Khalak and Williamson 1996; Jauvtis and Williamson 2004) and are shown in Table 1. As Table 1 illustrates, the reduced velocity is in the range which is equivalent to the Reynolds ($2 \times 10^3 < \mathrm{Re} < 13 \times 13^3$). According to the Fig. 5a (wherein the computational and experimental results are compared), it can be concluded when the reduced velocity reaches 4, the oscillation amplitude increases, which is named the VIV initial branch. As the reduced velocity passes 4, VIV enters the upper branch and then the lower branch and takes a downward trend. Eventually, vortexes disappear when the reduced velocity reaches the VIV reactions. According to Fig. 5b, the natural frequency and the vortex shedding frequency are combined and affect VIV frequency. In this figure, two curves are markedly, curve A is close to the natural frequency and mainly influenced by the natural frequency, and curve B is close to the vortex shedding frequency.

In general, when comparing this research data with the laboratory data, all three VIV branches show acceptable agreement. As illustrated in Fig. 5a, the upper branch of VIV in the present study exhibits a lower amplitude ratio

Fig. 3 Computational domain

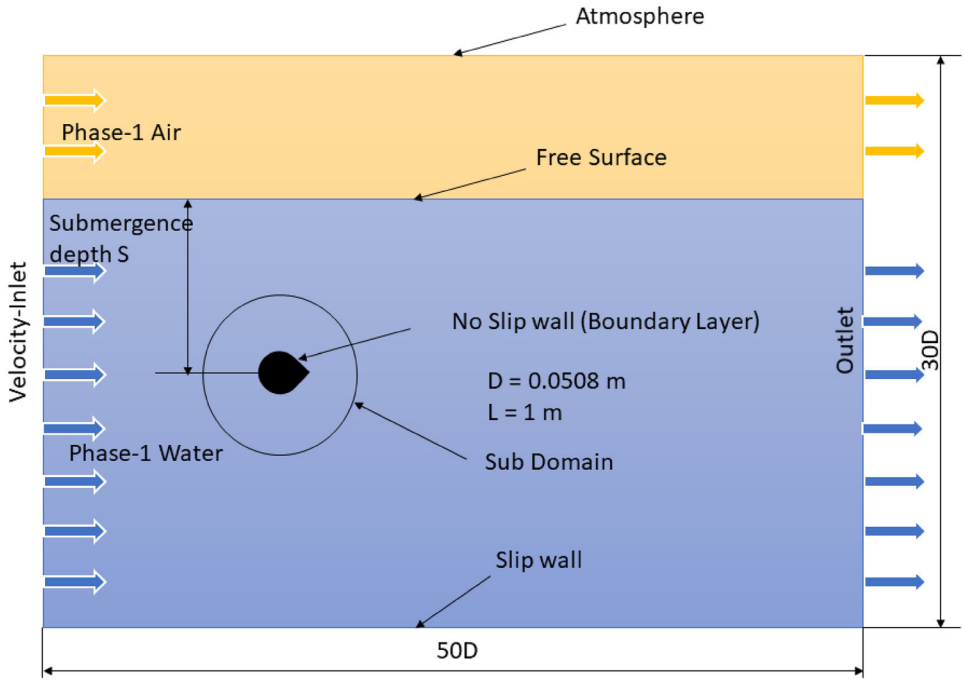

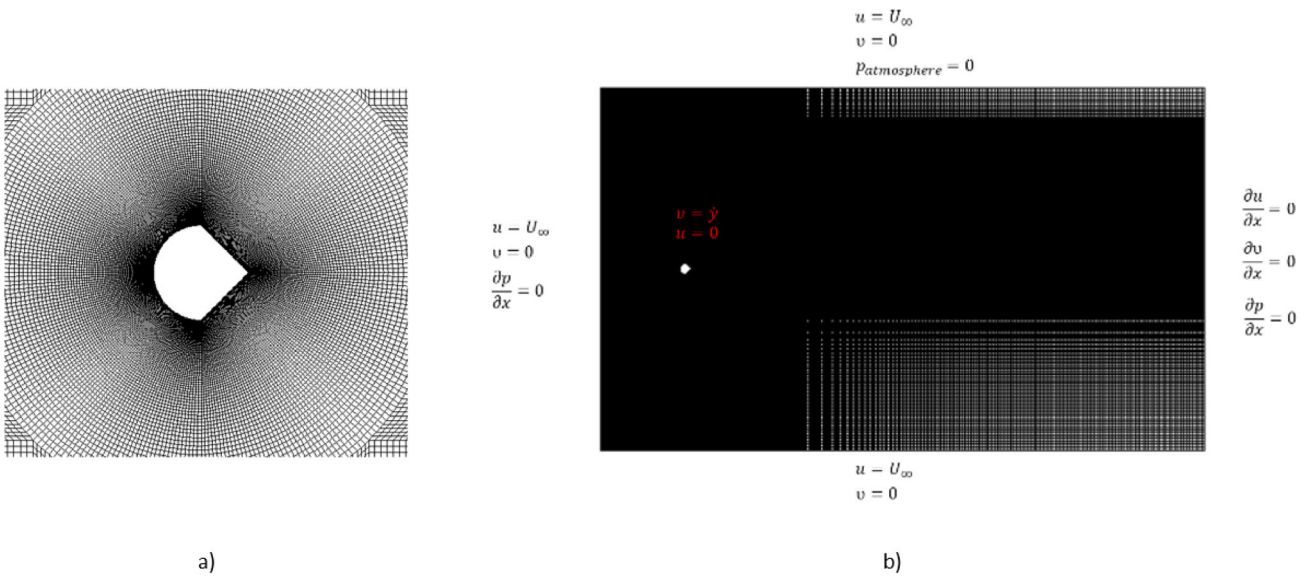

a) b)

Fig. 4 Grid configuration for the Cir-Tria Prism

compared to the laboratory results. This difference can be attributed to two main factors. First, in the experimental tests, the parameters of the VIV system are typically dimensionless or normalized (such as mass ratio, damping ratio, reduced velocity, etc.), which may affect the results. Second, the current study is based on a two-dimensional hypothesis, where the three-dimensional fluid is simulated without crossflow. This assumption neglects the strength of the lock-in point between the natural frequency and the vortex shedding frequency, leading to a reduced amplitude in the upper branch. Also, results of the previous studies which have been done computationally are like the present study (Guilmineau and Queutey 2004; Bernitsas 2016; Gu et al. 2020). Ultimately, the computational method of the present research has a reasonable convergence.

In this research, the sensitivity of the proposed numerical model in terms of choosing the Courant number (time step representative) with four different Courant numbers 0.8, 0.99, 1.4, 2 Fig. 6a, at the maximum Reynolds number (Re $= 13 \times 10^3$), has been investigated. For different Courant

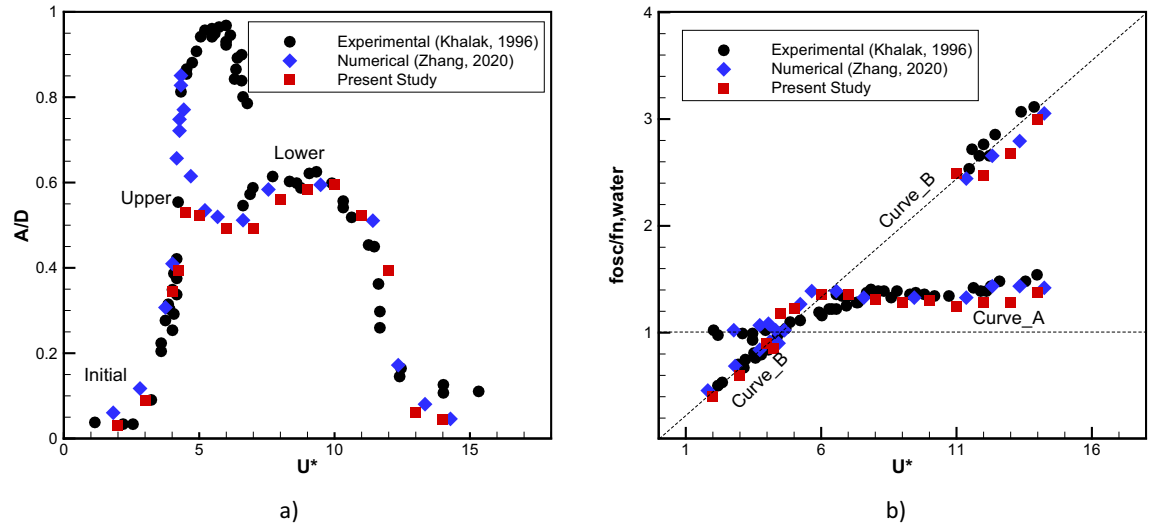

Fig. 5 Comparison of VIV responses for the numerical results and the experimental results

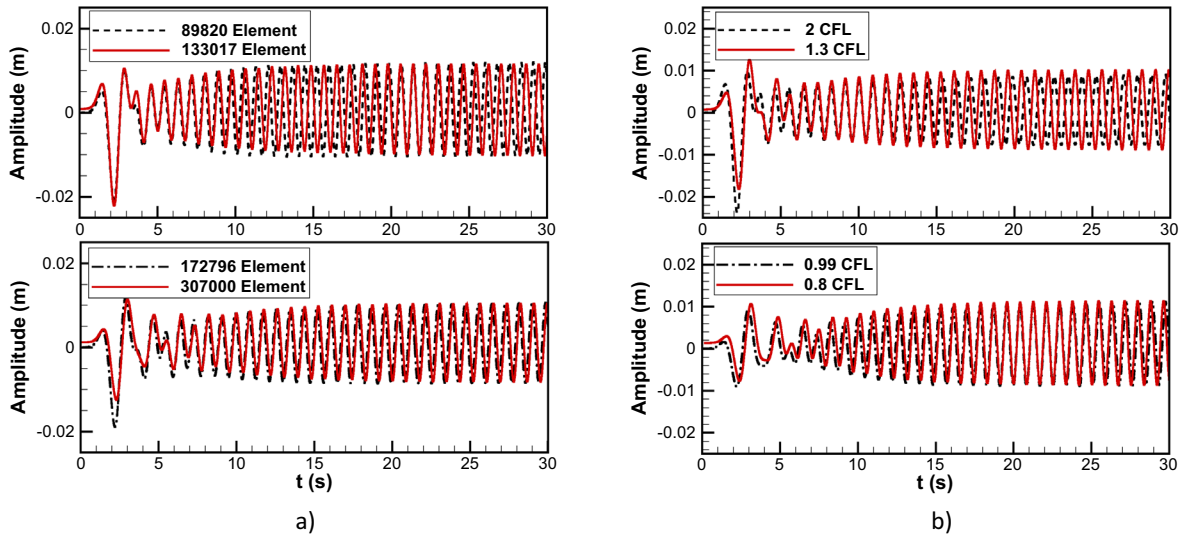

Fig. 6 **a** Time-step independence validation and **b** Grid sensitivity validation for a Cir-Tria Prism

numbers, the amplitudes tend to stabilize after 20 s, and also the amplitude's average relative error and the Cir-Tria prism oscillation frequency in two courants 0.99 and 0.8 equal to 1.32% and 0%, respectively. Based on this, considering the model sensitivity and the calculation efficiency, the 0.99 Courant number has been selected in the present research. Additionally, the sensitivity of the grid size study has been carried out by evaluating the amplitude responses with different grid densities. Four different grid densities with different numbers of computing cells are represented in Fig. 6(b), the average amplitude relative error and Cir-Tria prism oscillation frequency in two grids, 172,796 and 307,000 is 1.7% and 0%, respectively. Finally, to ensure the numerical simulation accuracy, average grid resolutions of 172,796 cells have been selected for the simulations. Also, according to the requirements of the K-Omega SST turbulence model, the grid near the cylinder wall should be small enough. As a result, the highest Reynolds number on the cylinder surface is approximately less than 1 (Gu et al. 2020).

5 Results

The sets of numerical simulations to investigate the Cir-Tria prism's FIM responses with different submergence depth ratios are represented in Fig. 7. Moreover, in Table 2 and Table 3, frequency ratio and amplitude ratio toward reduced flow velocity and submergence depth are summarized, respectively. As noticed in these tables, + + means

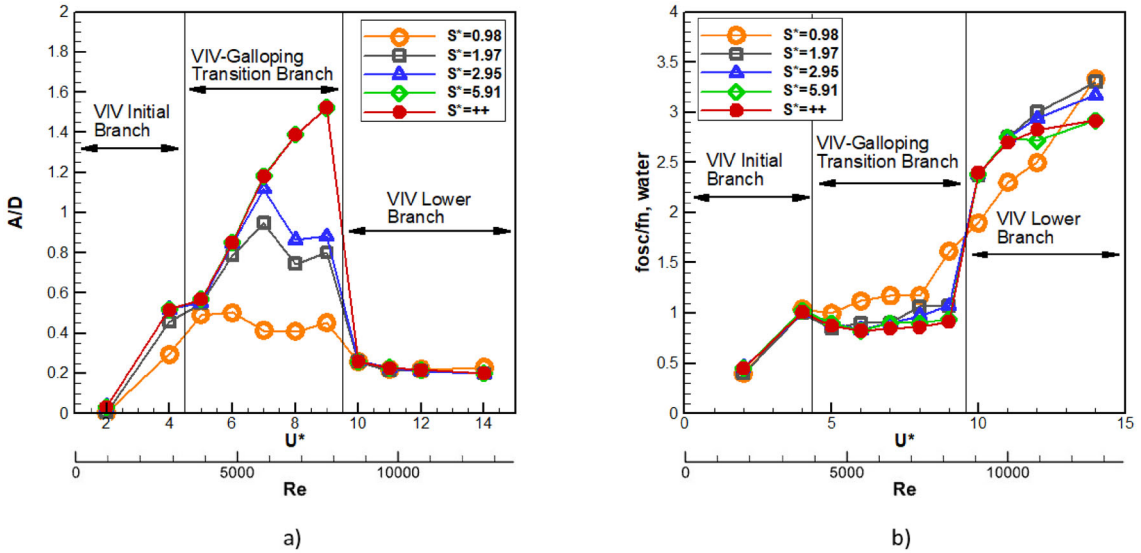

Fig. 7 **a** Amplitude ratio and **b** frequency ratio (f_{osc} /f_n) of the Cir-Tria Prism for different submergence depth ratios

Table 2 The FIM Amplitude ratio vs the flow Reduced velocity and Submergence depth

		S^* Submergence depth ratio				
		0.98	1.97	2.95	5.91	+ +
Reduced velocity	2	0.01	0.01	0.04	0.03	0.03
	4	0.30	0.47	0.54	0.52	0.52
	5	0.49	0.56	0.55	0.57	0.57
	6	0.50	0.79	0.85	0.85	0.85
	7	0.42	0.95	1.12	1.18	1.18
	8	0.42	0.74	0.86	1.38	1.39
	9	0.45	0.80	0.88	1.52	1.52
	10	0.25	0.25	0.26	0.26	0.26
	11	0.25	0.21	0.22	0.23	0.22
	12	0.25	0.21	0.22	0.23	0.22
	14	0.23	0.22	0.21	0.22	0.20

Table 3 The FIM frequency ratio vs the flow Reduced velocity and Submergence depth ratio

		S^* Submergence depth ratio				
		0.98	1.97	2.95	5.91	+ +
Reduced velocity	2	0.40	0.40	0.46	0.45	0.45
	4	1.04	1.00	1.01	1.03	1.01
	5	0.96	0.85	0.90	0.90	0.88
	6	1.13	0.90	0.84	0.83	0.83
	7	1.20	0.90	0.90	0.90	0.85
	8	1.18	1.10	0.98	0.98	0.86
	9	1.64	1.16	1.16	0.92	0.92
	10	1.90	2.40	2.40	2.40	2.40
	11	2.30	2.75	2.75	2.75	2.70
	12	2.50	3.00	2.94	2.72	2.83
	14	3.33	3.38	3.17	2.91	2.92

that the submergence depth is infinite and unlimited (single-phase flow) and this is considered as a point of reference. The reduced velocity ranges from 2 to 14. In the analysis of FIM branches, including the upper VIV branch, the transition (transition from VIV to galloping) and the lower VIV branch, the inputs are: flow velocity and submergence depth, and the outputs are: the magnitude of amplitude and frequency ratio. Based on this, the following brief results can be obtained.

Figure 7 illustrates that with an increase in the submergence depth of the Cir-Tria prism, there is a notable expansion in the spectrum of both VIV and galloping, along with an upward trend in their amplitudes. This observation suggests that proximity to the free surface dampens the prism's FIM response. However, when the depth ratio exceeds 5.91, the amplitude ratio stabilizes, indicating that beyond this threshold, the presence of the free surface ceases to significantly influence VIV and galloping.

This primary branch of VIV, depicted in Fig. 7, shows a gradual intensification of the VIV responses across all submergence depths. The tendency for an increase is consistently observed, indicating a robust relationship between VIV reactions and submergence depth. Moreover, changes in the amplitude ratio within this branch remain relatively uniform across different submergence depths, with the exception of the 0.98 depth ratio, which exhibits a distinct behavior.

Additionally, Fig. 7 shows the transition range from VIV to galloping. This critical range marks the termination of VIV and the commencement of galloping phenomena. The beginning of this range is characterized by an interference between VIV and galloping, signifying the transition from VIV to galloping as indicated by a decrease in FIM frequency. Moreover, the onset of the transition region is marked by more pronounced random fluctuation patterns. The analysis further reveals that a reduction in submergence depth leads to a decrease in the amplitude of galloping. Consequently, both the end of the transition phase and the extent of galloping diminish as the submergence depth decreases.

In the context of the lower VIV branch, shown in Fig. 7, the frequency of vortex shedding is observed to increase and diverge from the body's natural frequency. This divergence results in the decoupling of these frequencies, leading to a suppression of their amplitude. Additionally, across various submergence depths, the amplitude ratio curve for VIV maintains a nearly constant ratio, echoing the behavior seen in the initial branch.

From these cases, it can be concluded that the FIM responses is attenuated by reducing the submergence depth. This may be related to the vortex effects caused by the free-surface deformation.

6 FIM at low submergence depth

For submergence depth ratios $S^* = 1.97$ and $S^* = 2.95$ in the initial and lower VIV branches, the amplitude and frequency ratio, is almost near infinite depth as illustrated in Fig. 7. However, in the transition and galloping branches, FIM reactions are completely distinct from infinite depth. Since the most significant changes in the amplitude and frequency ratio for all three branches are seen in the ratio $S^* = 0.98$ of submergence depth, this ratio has been used for the VIV reaction analysis in the following three reduced flow velocities 4, 9, and 14; each of which took one of the initial, transition, and the lower branches of the infinite and unlimited submergence depth of the Cir-Tria prism, to be used as comparison reference, according to Fig. 7.

In the case where the reduced flow velocity is equal to 4, the FIM reaction occurs in the VIV initial branch. In this branch, the amplitude and oscillation frequency, both increase as Reynolds number increases (Fig. 7, initial branch). Also, the VIV frequency and amplitude equals to 0.4157 Hz and 0.0150 m, respectively. Figure 8 shows the amplitude and the lift coefficient, both in time and in other cases. By observing the lift force coefficient curve (blue curve) and the amplitude curve (red curve), the amplitude decreases in this region compared to the infinity submergence depth, and the decrease in amplitude is associated with weak growth in the VIV frequency. Figure 9 shows the vorticity contour field and the streamlines surrounding the prism. Since the oscillation amplitude and flow velocity are very low, the effects of the prism on free-surface deformation and free-surface on prism are not significant. However, partial effects are observed. There are two reasons why the FIM reactions are reduced and hence energy conversion is reduced. When free-surface deformation appears on a large scale, first, the vortex shedding frequency generated by the free surface is not synchronous with the vortex generated by the prism. Second, the vortices generated by the free surface and the top surface of the prism are in opposite directions (In Figs. 10, 12 and 14a, these opposing vortices are represented in different colors). Therefore, these two types of the vortex are gradually combined resulting in a reduction of the vortex intensity around the prism. In other words, the deformed free surface and the combined vortex cause a change in the pressure distribution around the prism and reduce the effective lift force on the cylinder, and lead to a reduction in FIM reactions because of energy conversion. Also, in this branch, the vortex formation pattern is typical of 2S mode: 2 single rotating vortexes, one rotates clockwise, and one rotates counterclockwise, which cast in a cycle, but the vortex that separates from the upper surface of the prism is neutralized and disappears by the vortex formed by the free surface.

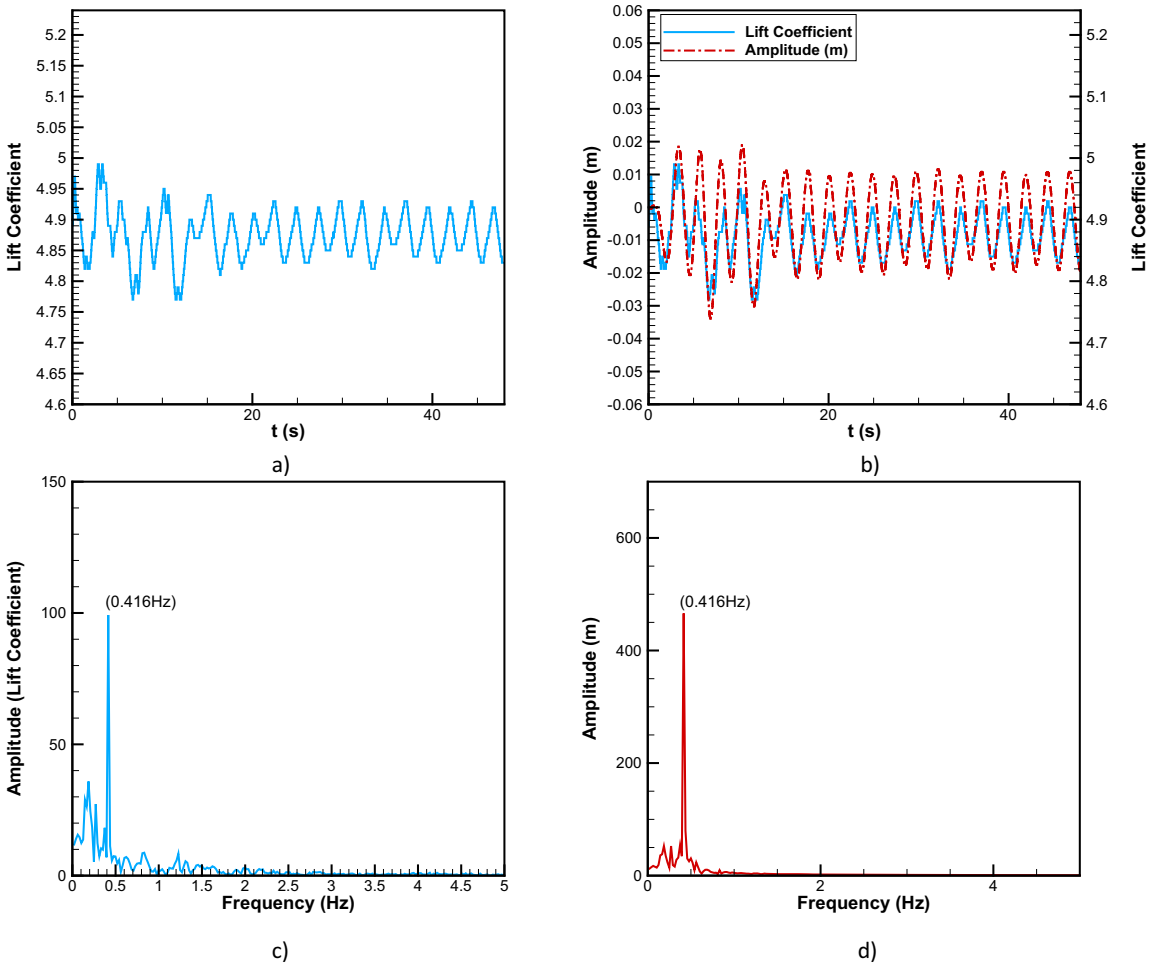

Fig. 8 **a** Lift coefficient versus time; **b** Amplitude response versus time; **c** Frequency spectrum for lift coefficient and (d) Frequency spectrum for amplitude of the Cir-Tria Prism with submergence depth ratio $S^* = 0.98$ at $U^* = 4$ (Re = 3621)

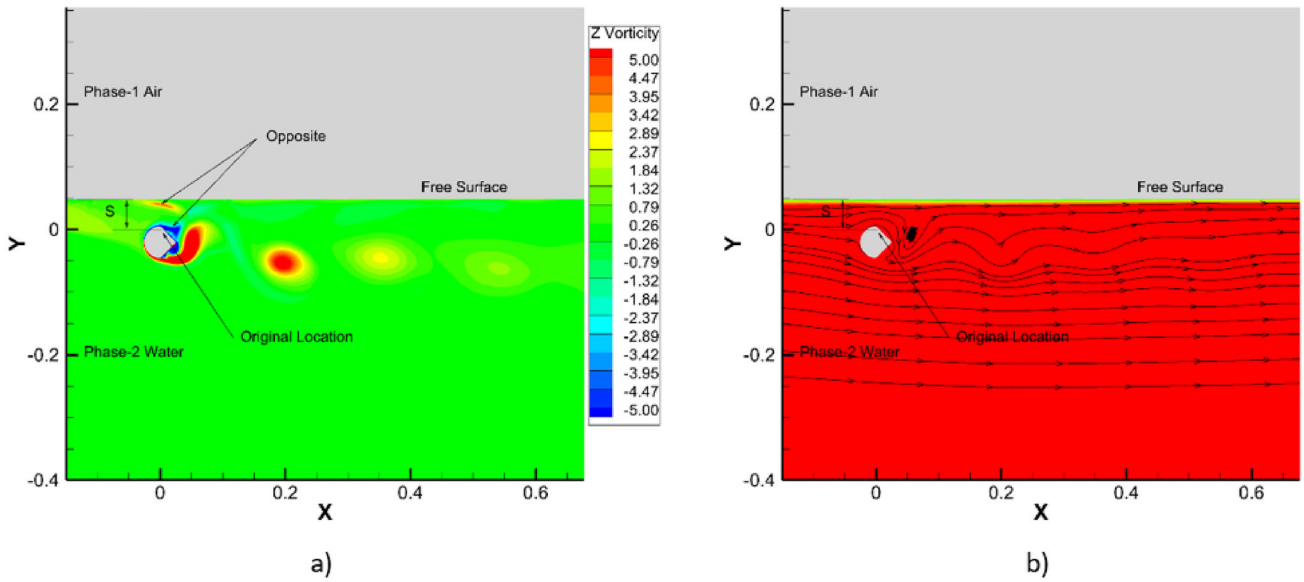

Fig. 9 **a** Vorticity field and **b** streamlines around the Prism with submergence depth ratio $S^* = 0.98$ at $U^* = 4$ (Re = 3621)

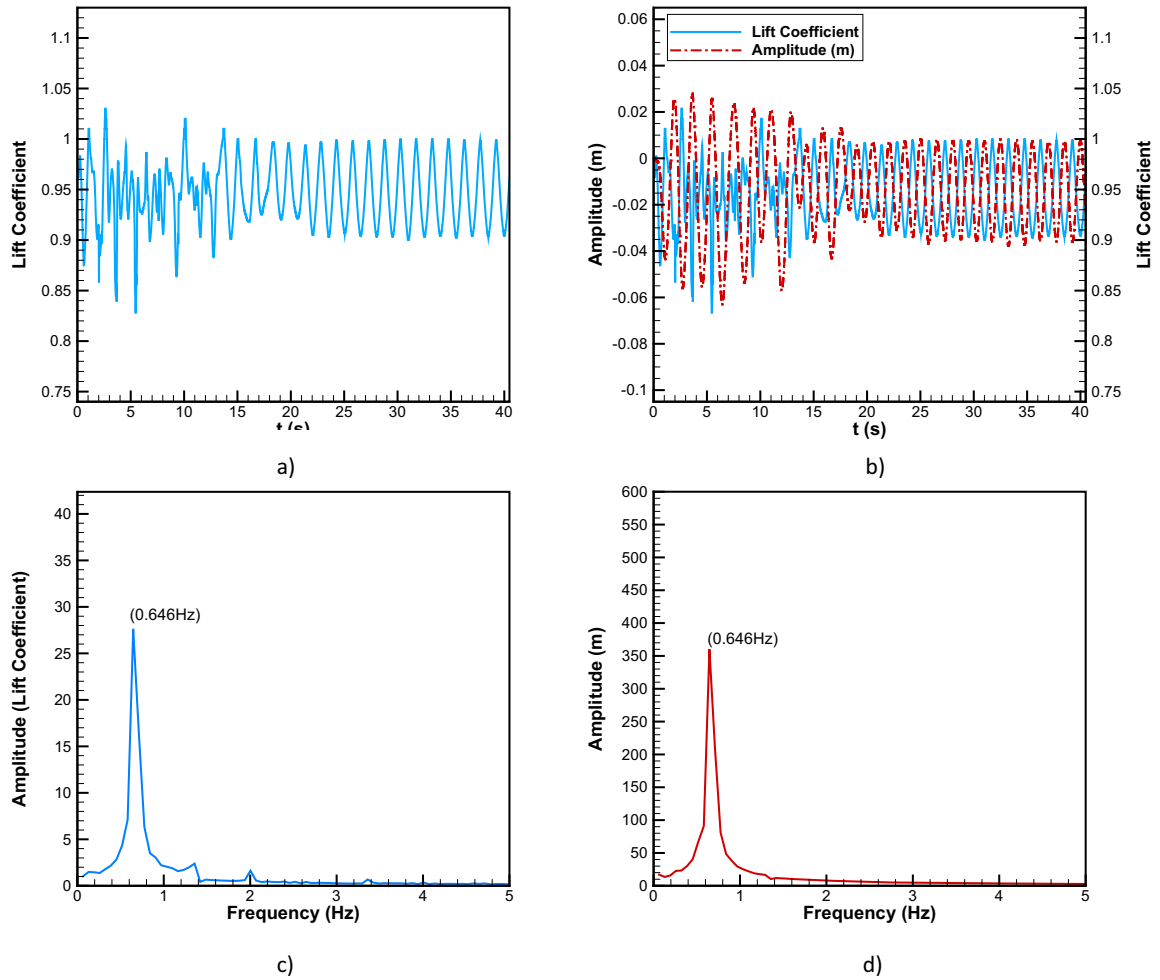

Fig. 10 **a** Lift coefficient versus time; **b** Amplitude response versus time; **c** Frequency spectrum for lift coefficient and (d) Frequency spectrum for amplitude of the Cir-Tria Prism with submergence depth ratio $S^* = 0.98$ at $U^* = 9$ (Re = 8149)

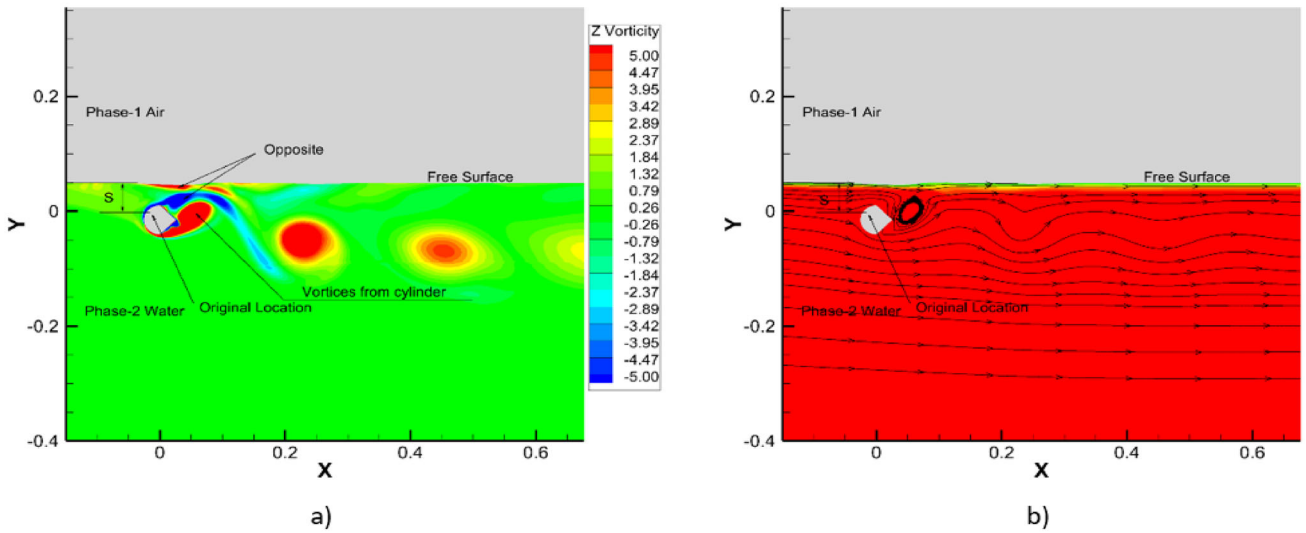

Fig. 11 **A** Vorticity field and **b** streamlines around the Prism with submergence depth ratio $S^* = 0.98$ at $U^* = 9$ (Re = 8149)

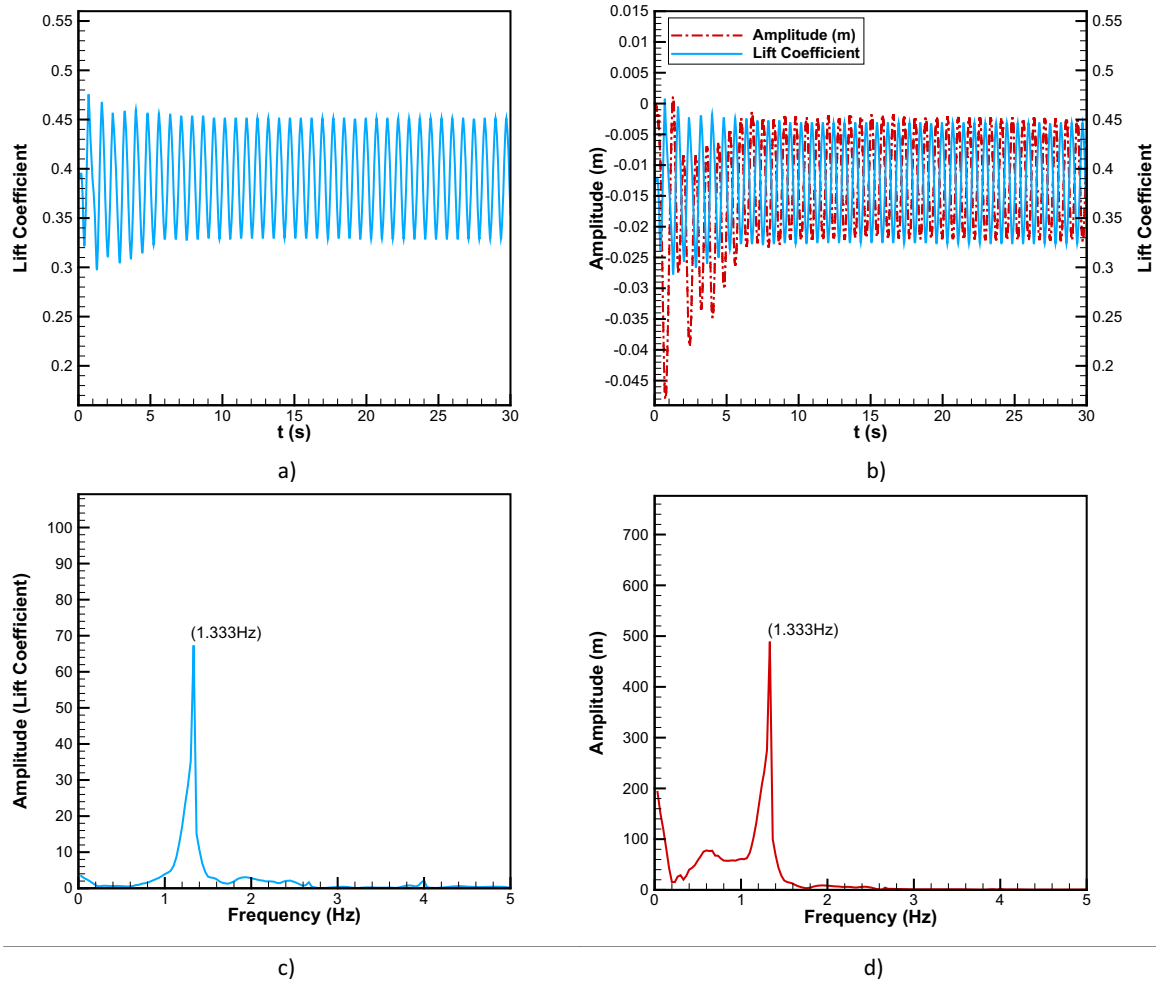

Fig. 12 **a** Lift coefficient versus time; **b** Amplitude response versus time; **c** Frequency spectrum for lift coefficient and (d) Frequency spectrum for amplitude of the Cir-Tria Prism with submergence depth ratio $S^* = 0.98$ at $U^* = 14$ (Re = 12,676)

In the case where the reduced flow velocity equals 9, the FIM response is a completely different example with infinite depth where galloping occurs. The galloping features are high amplitude and low frequency close to the natural frequency of the object. Also, fluid force changes more. However, the experiments show that the amplitude is greatly reduced and at the same time the frequency is increased. Therefore, the galloping movement is facilitated by reducing the submergence depth to be transferred to the VIV lower branch. (amplitude and lift coefficient are represented in terms of time). Figure 10 does not seem to belong to the galloping region. When the flow velocity increases, the free-surface deformation (wave creation phenomenon) increases, Fig. 11. The rotation direction of the two types of vortexes in Fig. 11 is opposite. So, the lift force resulting from the vortex shedding around the Cir-Tria prism also decreases. The FIM amplitude also decreases with the decrease of the submergence depth. The vortex formation pattern of this sample is a typical vortex formation mode (2S mode) (Williamson and Roshko 1988), and in this mode, there are 2 single rotational vortexes cast in a cycle (clockwise and counter clockwise). However, the vortex separated from the prism's upper surface is neutralized and disappears due to the vortex generated by the free surface.

In the case where the reduced flow velocity is equal to 14, the FIM reaction takes place in the lower branch of the VIV (according to Fig. 7, lower branch). In this branch, the shedding frequency increases steadily and deviates from the natural frequency. Thus, the VIV amplitude decreases, and the frequency and amplitude are equal to 1.333 Hz and 0.0117 m, respectively. The amplitude and lift force coefficient are shown in Fig. 12 in terms of time and other cases. By observing the lift force coefficient curve (blue curve) and

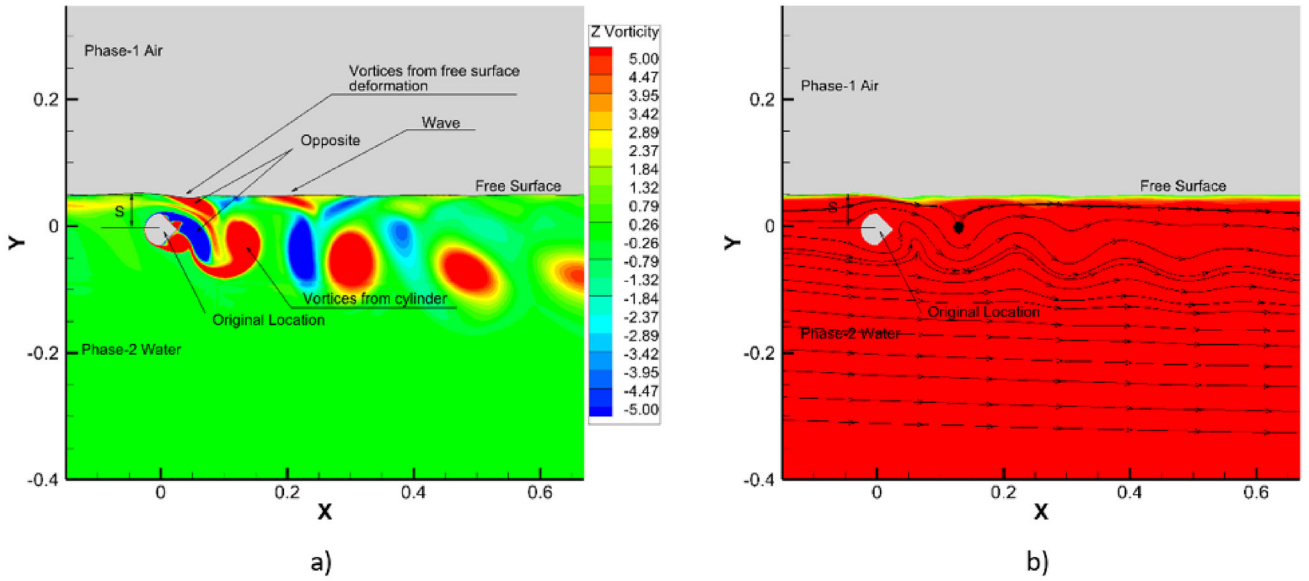

Fig. 13 **a** Vorticity field and **b** streamlines around the Prism with submergence depth ratio $S^* = 0.98$ at $U^* = 14$ (Re = 12,676)

the amplitude curve (red curve), the peaks of lift force have a phase difference with the amplitude curve peaks but share the same period. Therefore, the Cir-Tria prism FIM response is considered VIV. Figure 13 shows the vector field and flow line around the prism. A typical 2S vortex shedding mode for the FIM of a Cir-Tria prism at Reynolds 12,676, in the VIV lower branch, is observed. The free-surface deformation and the wave creation phenomenon are observed in this sample, very similar to the numerical results obtained for the circular by (Gu et al. 2020). It appears that the submergence depth and the flow velocity can be considered two effective factors in altering the formation of the free surface.

The above results indicate that the VIV amplitude at the low submergence depth is relatively small. The reasons for this are as follows: in general, two types of vortices co-exist in the flow, the vortices shed from the prism shear layer and the vortices produced by deformed free surfaces. The first type of vortices creates the force that drives the prism's galloping or VIV reactions. Also, the free surface deformation due to the pressure fluctuations between the free surface and the prism, creates a series of vortices that are the second type of vortices. Also, the vortex pattern in all three cases is significantly similar.

7 FIM at high submergence depth

When the submergence depth ratio reaches $S^* = 5.91$ (Fig. 7), the amount of energy conversion and VIV amplitude no longer increases. In other words, the submergence depth becomes unlimited. This means when it is $S^* = 5.91$, the submergence depth or the influence of the free surface can be ignored. Therefore, $S^* = 2.95$ was selected as a case study for three reduced flow velocities 4, 9, and 14, each located in one of the FIM branches at high submergence depth.

If the reduced flow velocity is 4, then the FIM reaction takes place in the initial branch of the VIV. In this initial branch, both the amplitude and the oscillation frequency increase as Reynolds increases (Fig. 7, initial branch). Also, the VIV frequency and amplitude equal 0.402 Hz and 0.0273 m, respectively. This means that the amplitude is not sensitive to the flow velocity at high submergence depths, unlike the cases for the shallow submergence depth. Figure 14 shows the amplitude and lift force coefficient in time and other cases. The blue curve shows the lift force coefficient curve, and the red curve shows the amplitude curve. The peaks of the lift force correspond to the peak of the amplitude curve. Since the amplitude curve follows the lift force curve, the amplitude curve is considered to be VIV. The vector field and flow lines surrounding the prism are represented in Fig. 15. Due to the high submergence depth and very low flow velocity, neither the cylinder's effect on free surface deformation nor the free surface's effect on Cir-Tria prisms can be observed in this branch. Therefore, the effects due to the free surface are negligible and can be disregarded. In previous studies (Williamson and Roshko 1988; Williamson and Jauvtis 2004; Ding et al. 2015), different vortex patterns related to different FIM regions have been classified as [2S] (S = single), [2P] (P = pair), [nP + nS], etc. In the initial VIV branch, a typical 2P vortex shedding mode for FIM at Reynolds 3621 Cir-Tria prism is observed, which means two vortex pairs per cycle.

At reduced flow velocity 9, the FIM response is completely different with infinite depth; we have already shown that at this depth, galloping occurs. Galloping has a high amplitude

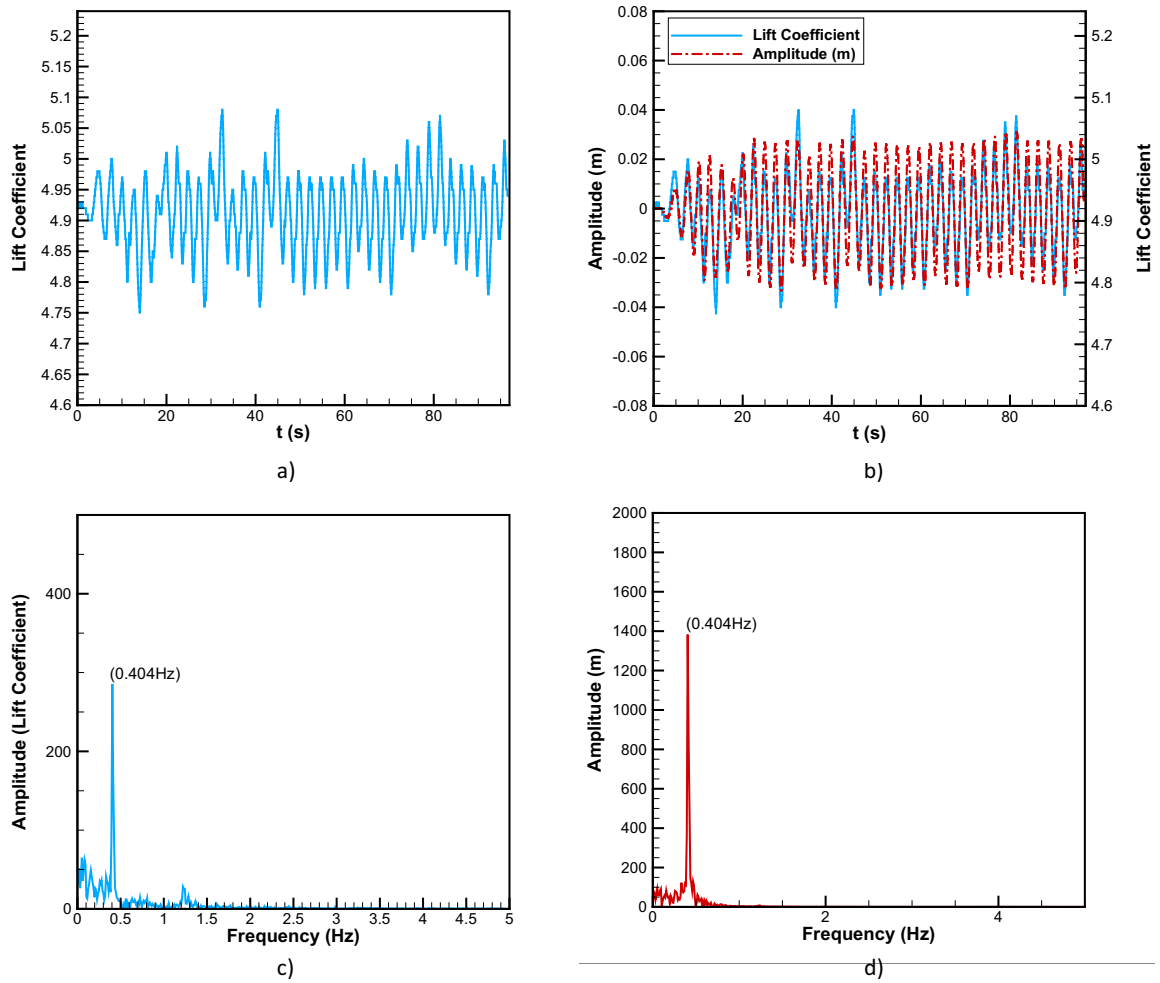

Fig. 14 **a** Lift coefficient versus time; **b** Amplitude response versus time; **c** Frequency spectrum for lift coefficient and **d** Frequency spectrum for amplitude of the Cir-Tria Prism with submergence depth ratio $S^* = 2.95$ at $U^* = 4$ (Re = 3621)

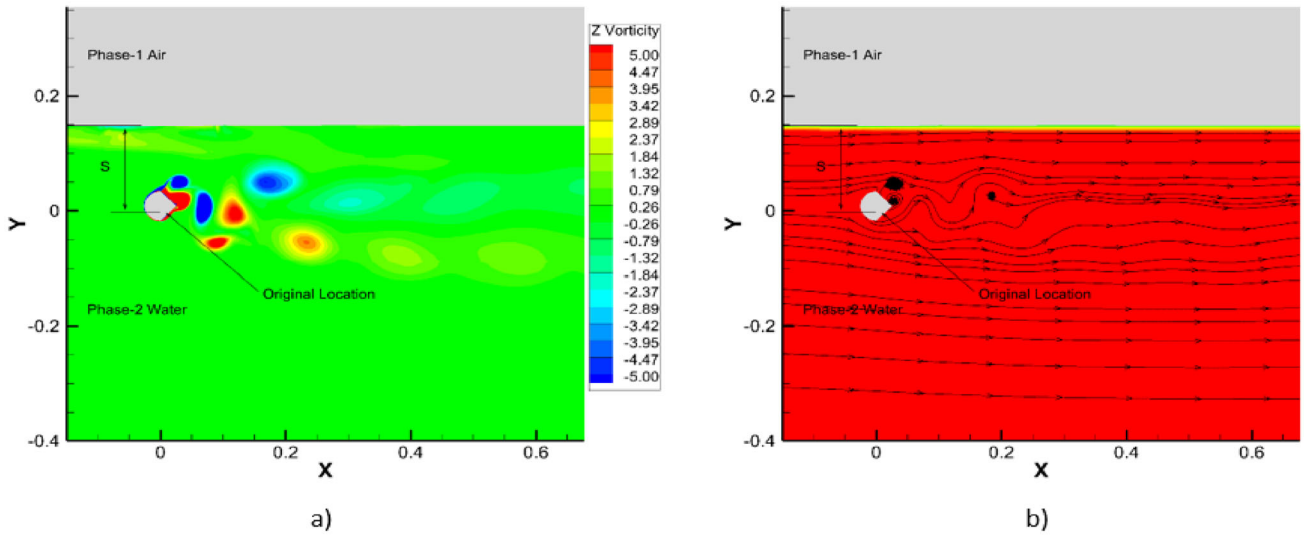

Fig. 15 **a** Vorticity field and **b** streamlines around the Prism with submergence depth ratio $S^* = 2.95$ at $U^* = 4$ (Re = 3621)

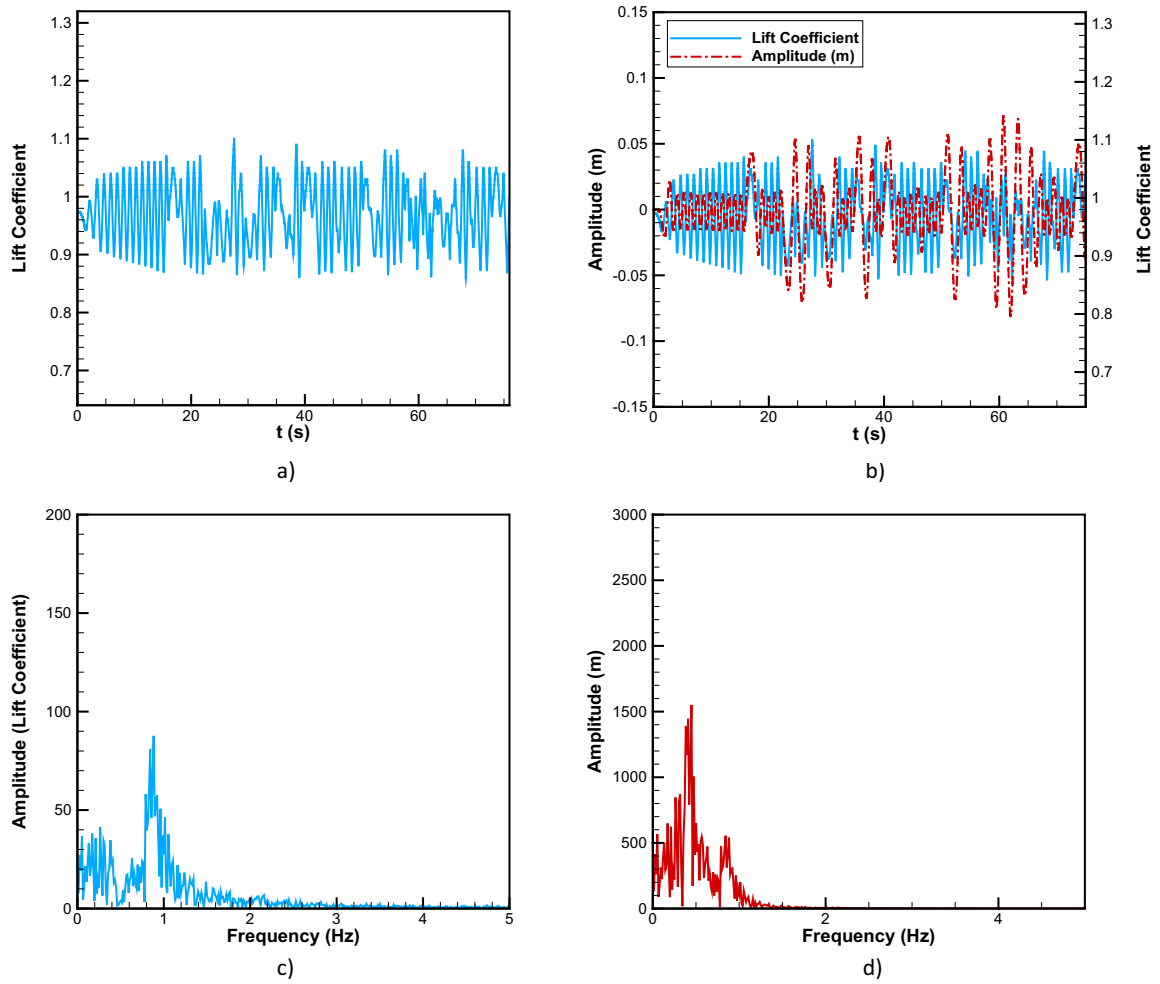

Fig. 16 **a** Lift coefficient versus time; **b** Amplitude response versus time; **c** Frequency spectrum for lift coefficient and **d** Frequency spectrum for amplitude of the Cir-Tria Prism with submergence depth ratio $S^* = 2.95$ at $U^* = 9$ (Re = 8149)

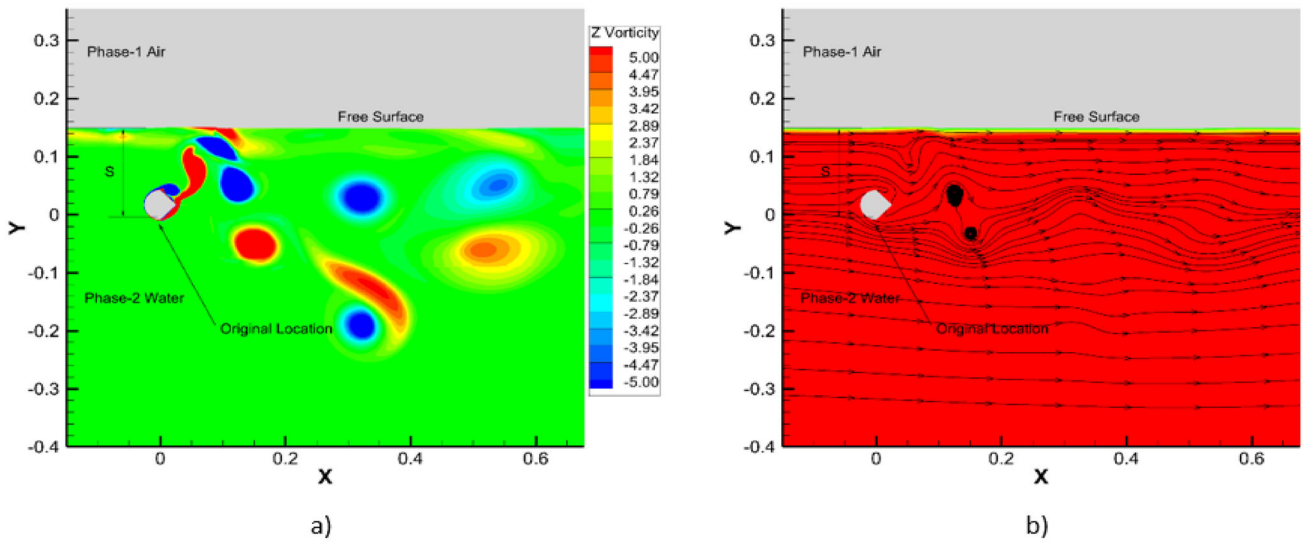

Fig. 17 **a** Vorticity field and **b** streamlines around the Prism with submergence depth ratio $S^* = 2.95$ at $U^* = 9$ (Re = 8149)

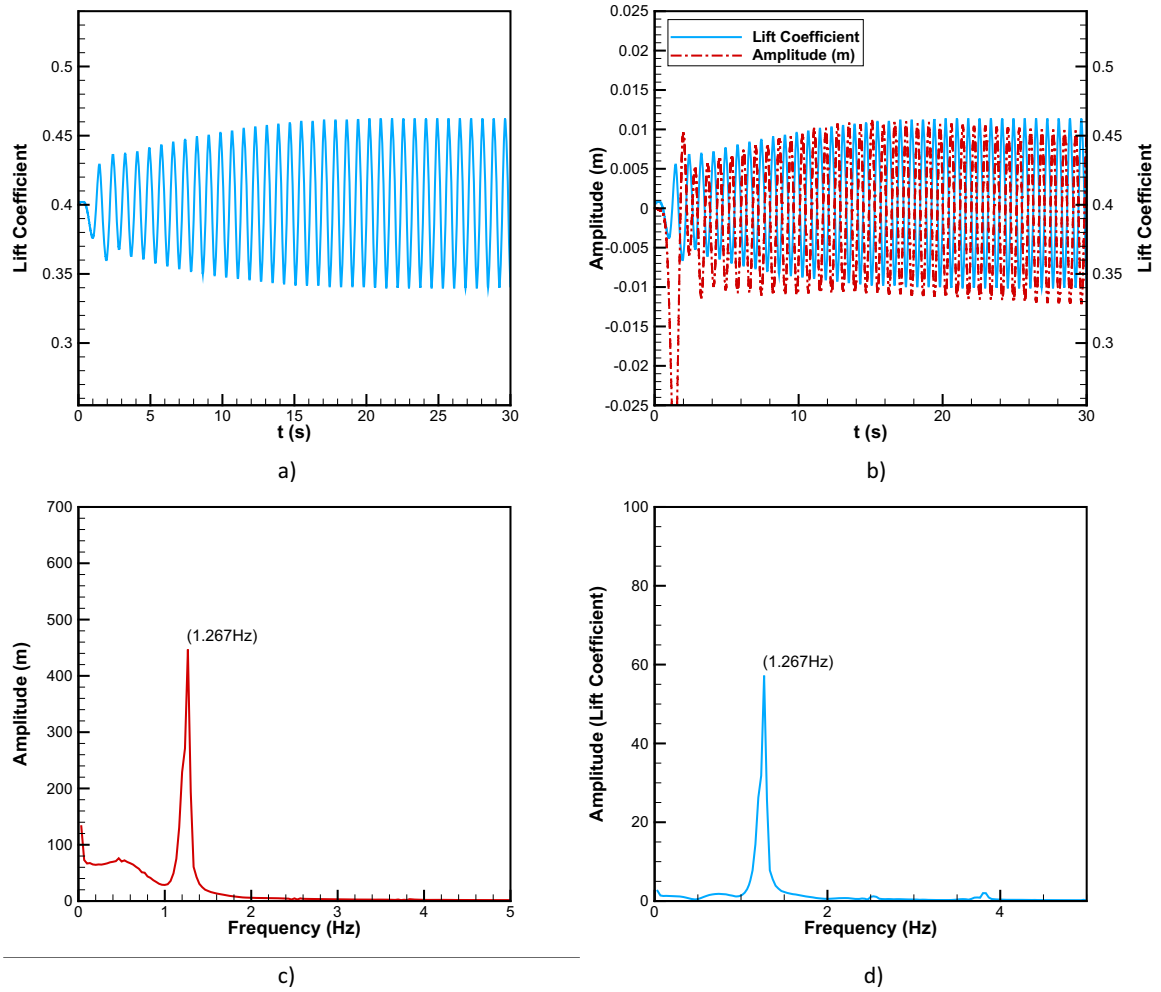

Fig. 18 **a** Lift coefficient versus time; **b** Amplitude response versus time; **c** Frequency spectrum for lift coefficient and **d** Frequency spectrum for amplitude of the Cir-Tria Prism with submergence depth ratio $S^* = 2.95$ at $U^* = 14$ (Re = 12,676)

and low frequency close to the object's natural frequency. Fluid force changes more in this case. However, numerical results show that in this case study, there are two amplitudes. Also, the frequency is variable, so it does not belong to the galloping region. It is a median sample between galloping and the lower branch of VIV. (The amplitude and lift force coefficient represented in Fig. 16, in terms of time and other cases). Figure 17 shows the vector field and the flow lines around the prism. Since the vortex pattern is median, it is impossible to describe this case study.

The FIM reaction occurs at reduced flow velocity 14 at the lower branch of the VIV. The shedding frequency increases continuously in this branch, deviating from the natural frequency (Fig. 7, lower branch). As a result, the VIV amplitude decreases. The frequency and the amplitude of VIV are 1.2667 Hz and 0.0108 m, respectively. The amplitude and the lift force coefficient in time and other cases are illustrated in Fig. 18: Observing the lift force coefficient curve (blue) and the amplitude curve (red), it is evident that lift force peaks show a phase difference with amplitude curve peaks, but share the same periodicity. Cir-Tria vortex FIM response is therefore considered to be VIV. To gain a better understanding of the prism dynamics, the vortex structures are presented after CFD post-processing. The vector field and flow lines surrounding the cylinder are illustrated in Fig. 19. In the lower branch of VIV, a typical vortex shedding mode 2S for FIM at 12,676 Reynolds at a Cir-Tria prism is observed. This means two single clockwise rotating vortices and one counter clockwise rotating vortex are shed per cycle; This phenomenon is analogous to von Kármán vortex street.

FIM at unlimited submergence depth

The three reduced flow velocities 4, 9, and 14, correspond to the initial VIV branch, the transition region, and the lower

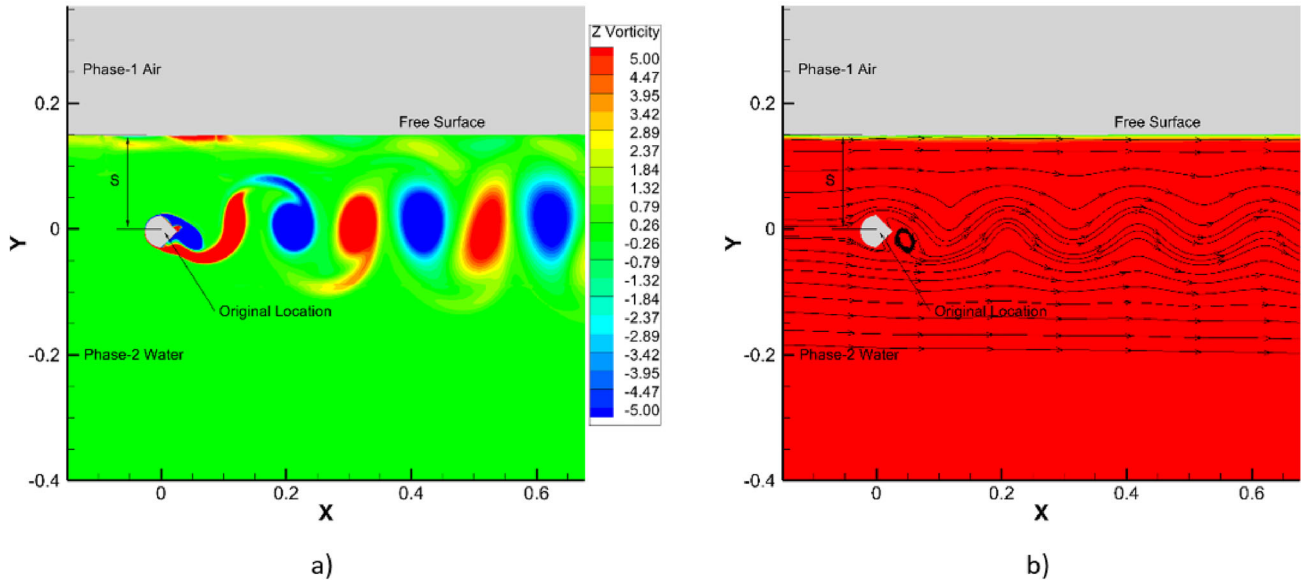

Fig. 19 **a** Vorticity field and **b** streamlines around the Prism with submergence depth ratio $S^* = 2.95$ at $U^* = 14$ (Re = 12,676)

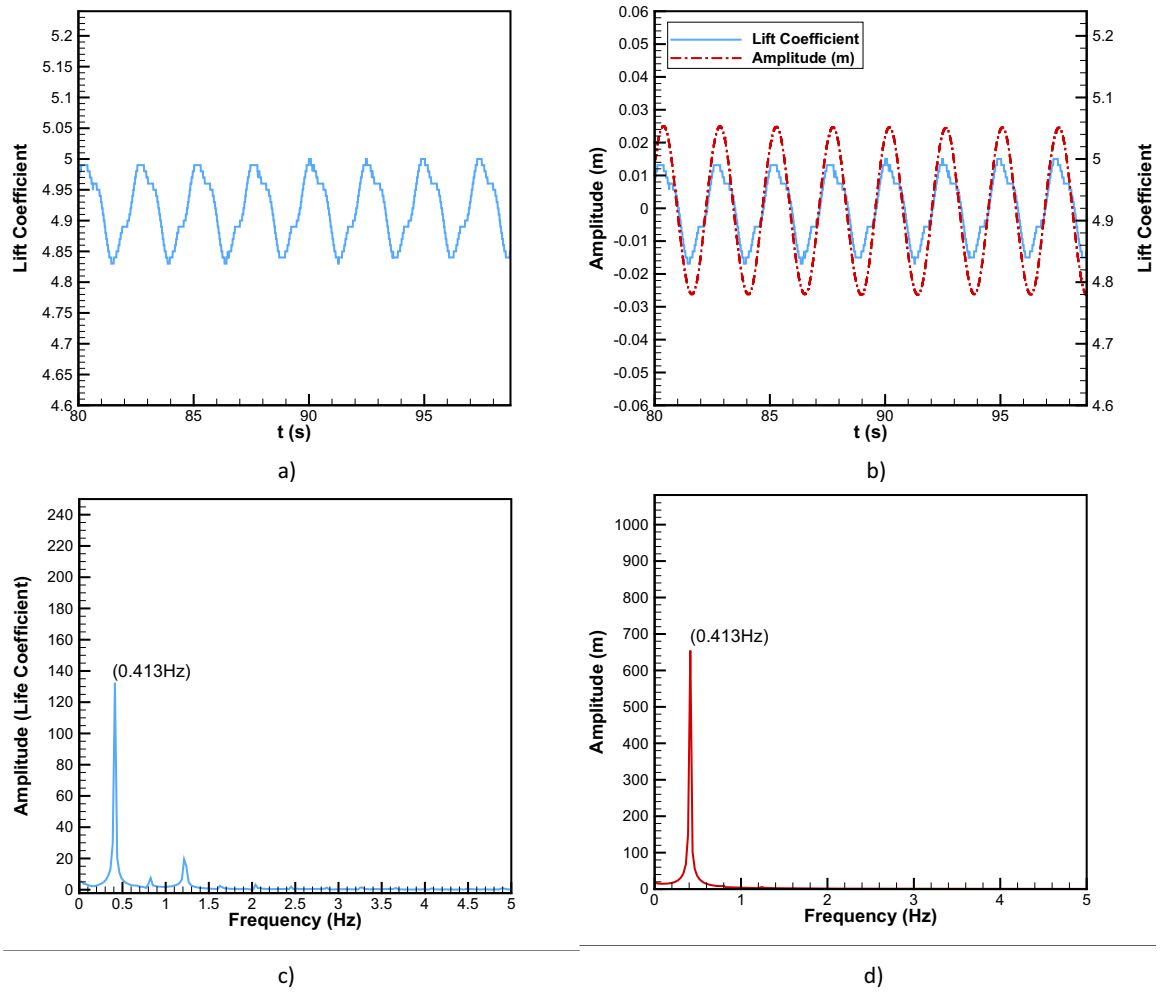

Fig. 20 **a** Lift coefficient versus time; **b** Amplitude response versus time; **c** Frequency spectrum for lift coefficient and **d** Frequency spectrum for amplitude of the Cir-Tria Prism with submergence depth ratio $S^* = + +$ at $U^* = 4$ (Re = 3621)

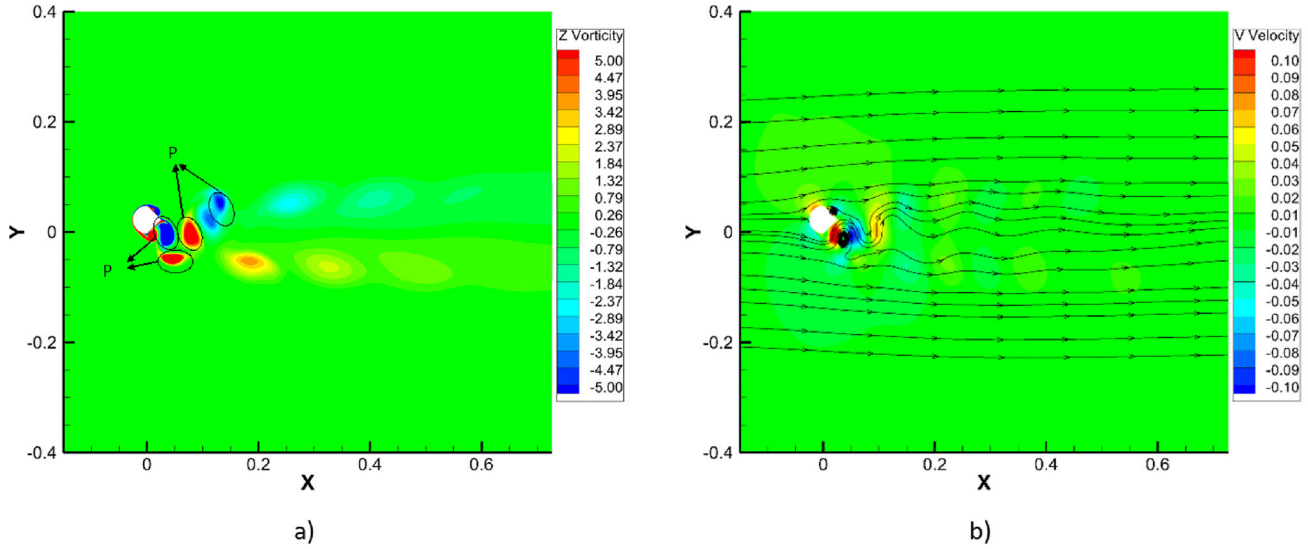

Fig. 21 **a** Vorticity field and **b** streamlines around the Prism with submergence depth ratio $S^* = + +$ at $U^* = 4$ (Re = 3621)

VIV branch, respectively (Cir-Tria, Fig. 7). These velocities were chosen to closely examine and analyze the behavior of the FIM branches.

At the reduced velocity of 4, then the FIM reaction takes place in the region of the initial VIV branch. Within this branch, both the amplitude and the oscillation frequency increase as Reynolds increases. The VIV frequency and amplitude also equal (0.413 Hz) and (0.025 m), respectively, according to Fig. 20a, d. The amplitude and the lift coefficient are expressed in time in Fig. 8. Observe the lift coefficient curve (blue) and the amplitude curve (red). The peaks of the lift force correspond to the peaks of the amplitude curve. Hence, the amplitude curve follows the same trend as the lift force coefficient curve. The Cir-Tria FIM response is, therefore, considered VIV. Figure 21 shows the vector field and flow lines around the prism. In previous studies (Williamson and Roshko 1988; Williamson and Jauvtis 2004; Rostami and Armandei 2017), different vortex patterns related to different FIM regions were named 2S (S = single), 2P (P = pair), nP + nS, etc. The initial VIV branch shows a typical 2P vortex shedding mode for the CIR-Tria prism FIM at the Reynolds 3621, i.e., two pairs are shed per cycle.

At the reduced velocity of 9, the FIM reaction occurs in the galloping branch. High amplitude and low frequency are characteristics of galloping, which is close to the natural object frequency. As Reynolds number increases in this branch, the amplitude increases and the frequency remains constant. The galloping frequency is 0.357 Hz, and the amplitude is 0.075 m (Fig. 22a, d). The amplitude and the lift force coefficient are represented in Fig. 22 for time and other cases observe the lift coefficient curve (blue) and the amplitude curve (red). For the prism, the lift force coefficient changes more than once in a single cycle. Therefore, the amplitude curve does not follow the same linear trend as the lift coefficient curve. Thus, the Cir-Tria FIM response is considered to be galloping. To better understand the dynamics of the Cir-Tria prism, the vortex structures are presented post-processing CFD. Figure 23 shows the vector field and flow lines surrounding the prism. The number of shed vortices is significantly higher compared to VIV In the galloping region. Geometrically asymmetric flow has been shown to be a major contributing factor to galloping (Bernitsas 2016). The 2S pattern is not the only vortex pattern related to the FIM regions. For instance, the 2P vortex pattern, nP + nS vortex pattern, etc. can be defined according to studies (Ding et al. 2015). The pattern of shed vortices for the Cir-Tria prism in the downward trend is first, three vortices, a single vortex, and a paired vortex, followed by a single vortex. The order of vortex shedding in each half cycle is P + S + S. The same P + S + S sequence of shedding is also observed in the upward trend. Therefore, the vortex pattern can be obtained in a galloping cycle of 2P + 4S, as shown in Fig. 23a.

At the reduced velocity of 14, the FIM reaction occurs in the lower VIV branch. In this branch, the shedding frequency increases continuously and deviates from the natural frequency, so the VIV amplitude decreases. Also, the VIV frequency and amplitude equal 1.2 Hz and 0.01 m, respectively. The amplitude and the lift force coefficient are represented in Fig. 24 in terms of time and other cases. Observe the lift force coefficient curve in blue and the amplitude curve in red. The lift force peaks have a phase difference from the amplitude curve peaks. However, they have the same

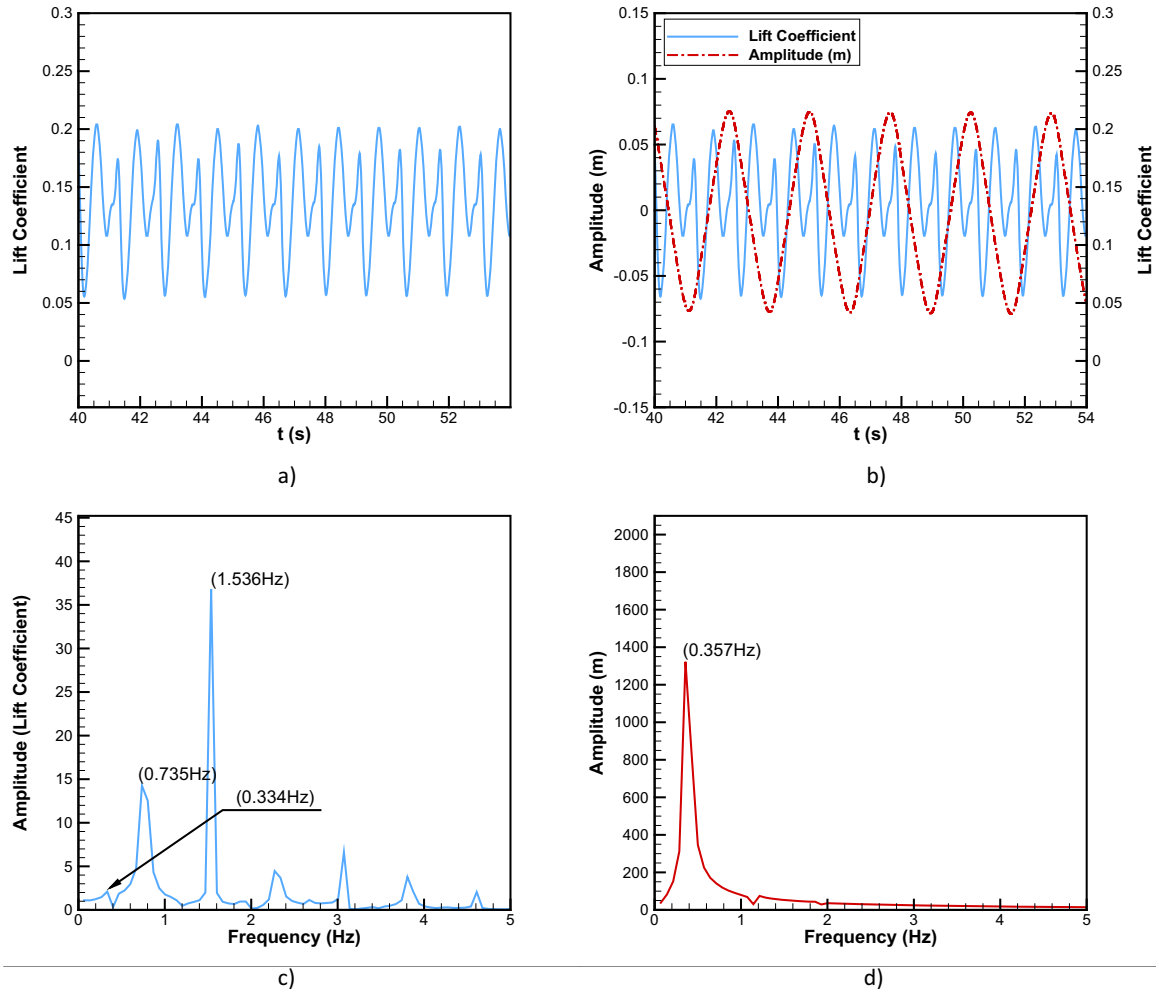

Fig. 22 **a** Lift coefficient versus time; **b** Amplitude response versus time; **c** Frequency spectrum for lift coefficient and **d** Frequency spectrum for amplitude of the Cir-Tria Prism with submergence depth ratio $S^* = + +$ at $U^* = 9$ (Re = 8149)

period. Therefore, the FIM response of the Cir-Tria prism is considered to be VIV. Figure 25 illustrates the vector field and flow lines surrounding the cylinder. In the lower VIV branch, for the Cir-Tria FIM at Reynolds 12,676, a typical 2S vortex shedding mode is observed, which means two rotating single vortices rotating clockwise and counterclockwise. The vortexes are shed in a cycle. This phenomenon is similar to the von Kármán vortex street.

8 Energy conversion

Another aim of the current study is to examine the variation in energy conversion. A cir-tria geometry is selected to replace the conventional circular cylinder, and an initial comparison is made between both geometries at infinite submergence depth. This comparison, as shown in the Fig. 26.

According to the results, the cir-tria shows a significantly larger output power especially in moderate reduced velocities due to larger vibration amplitude. Comparing the efficiency shows pick at $U^* = 4$, lower values for $U^* = 5$–6 and higher efficiencies at $U^* = 7$–9. Comprehending how submergence depth affects energy conversion is essential for understanding the dynamics of the FIM power conversion system. Figure 27 displays the power conversion results for different submergence depths ranging from 0.98 to 5.91 and higher, calculated using Eq. (3). The study shows that the initial VIV branch consistently increases converted power at all submergence

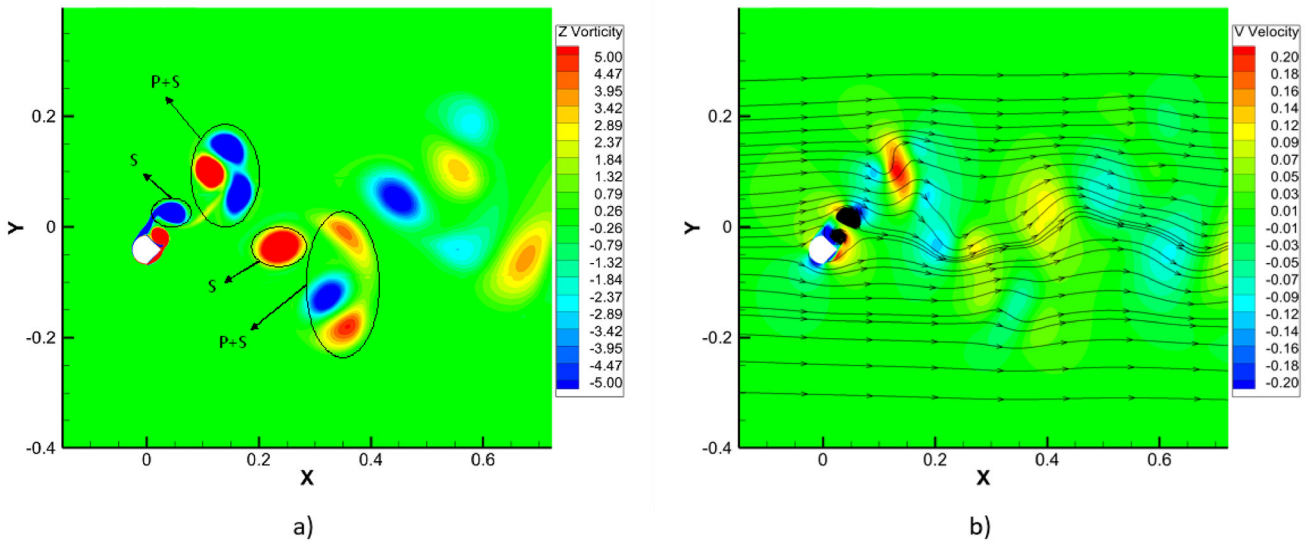

Fig. 23 **a** Vorticity field and **b** streamlines around the Prism with submergence depth ratio $S^* = ++$ at $U^* = 9$ (Re = 8149)

depths, with the best efficiency seen in this branch. However, there are moderate variations in the power curves at a submergence depth of 0.98.

In branches where the transition to galloping occurs, the power conversion diagram reaches its peak when the submergence depth is infinite. This suggests that the extracted power falls as the depth of submergence decreases, that supports earlier findings on section "FIM at low submergence depth". In the lower VIV branch, the effect of submergence depth on oscillation amplitude is minor. There is a slight increase in oscillation amplitude and therefore in output power as the submergence depth decreases.

Converted power is often lower at moderate submergence depths than at deeper depths. The drop in power can be linked to the distortion of the free surface, resulting in less lift force on the cylinder and absorption of kinetic energy from the fluid, causing energy dissipation. A reduction in submergence depth results in a decrease in converted power in this scenario.

When analyzing energy conversion performance and efficiency with Eq. (9) from Fig. 28, it is clear that efficiency increases in the beginning and reaches its maximum at that point. The efficiency curves in this early VIV branch are well-aligned, indicating that the submergence depth has little effect on efficiency. The research shows that the largest power production occurs in the galloping branch at infinite depth, whereas the greatest efficiency is observed in the initial VIV branch, also at infinite depth.

9 Conclusion

This study investigates the impact of submergence depth on the oscillatory and frequency responses of the Cir-Tria configuration, as well as its power generation and efficiency. These parameters are analyzed within a specified Reynolds number range and at reduced velocities from 2 to 14. The analysis is conducted using a C + + code-based computational fluid dynamics approach, implemented within the OpenFOAM framework. The research employs the unsteady, incompressible Navier–Stokes equations in conjunction with the K-omega SST turbulence model, the two-phase Volume of Fluid (VOF) model, and the spring–damper–mass system. The numerical findings are corroborated by empirical and experimental data to ensure validity and accuracy. The main findings of the present research are summarized as follows:

1. In general, as the submergence depth decreases and the object gets close to the flow surface, the FIM amplitude decreases and results in a similar decrease in the hydrokinetic energy conversion. Compared to high submergence depths, when the submergence depth ratio is 0.98, the FIM amplitude is significantly suppressed. At this point, the maximum amplitude ratio is only 0.50. Meanwhile, the responses range of FIM is also shortened. Reducing the submergence depth and proximity to the flow surface negatively impacts the FIM response due to the interaction between vortices generated by the flow surface and those from the prism's upper shear layer. The interaction between these counter-rotating vortices weakens and even neutralizes the effect of the upper vortices on the object, resulting in a change in the flow structure around the prism and the governing FIM phenomena.

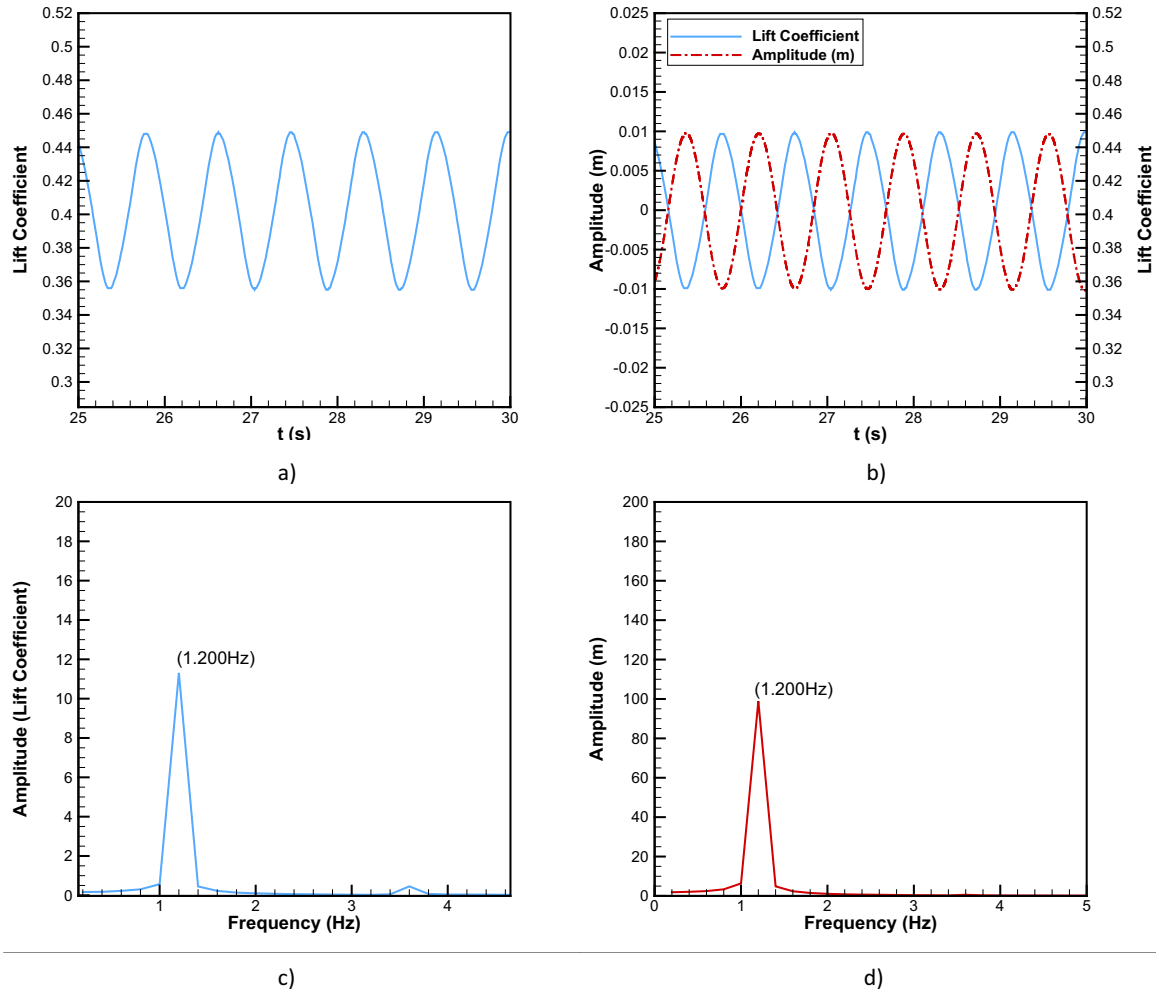

Fig. 24 **a** Lift coefficient versus time; **b** Amplitude response versus time; **c** Frequency spectrum for lift coefficient and **d** Frequency spectrum for amplitude of the Cir-Tria Prism with submergence depth ratio $S^* = + +$ at $U^* = 14$ (Re = 12,676)

2. The VIV initial branch is first observed as the flow velocity increases. The VIV responses gradually become strong. The vortex shedding is 2P pattern. In the transition range from VIV to galloping, the maximum amplitude ratio reaches up to 1.52 and the vortex shedding pattern is found to be 2P + 4S. In the VIV lower branch, the amplitude decreases to zero. Accordingly, the converted power and energy conversion efficiency approaches zero. In this case, which shows a 2S vortex shedding pattern (two single vortex in a shedding cycle) presented in Fig. 25a, the oscillating cylinder produces a small amount of energy, which poses no application value in practical application.

3. For all the submergence depth in the initial branch of VIV, the converted power increases as the flow velocity increases. The maximum power appears in the transition range from VIV to galloping and reaches up to about 2.7×10^{-3} W. The converted power starts decreasing in the lower branch. As the submergence depth increases with the same velocity, the converted power keeps increasing. Therefore, a Cir-Tria Prisms at higher submergence depths of 5.91 can be positively exploited for the FIM energy conversion system.

4. The energy conversion efficiency increases with the increasing flow velocity. After the VIV initial branch, the efficiency starts to decrease. As the submergence depth ratio increases from 0.98 to 5.91, the maximum efficiency keeps increasing. Finally, the maximum energy conversion efficiency reaches up to 1.4%. The efficiency curve at the submergence depth ratio of 5.91 coincides many times with the efficiency curve at the ratio of + + , which means the effects of submergence depth has become negligible.

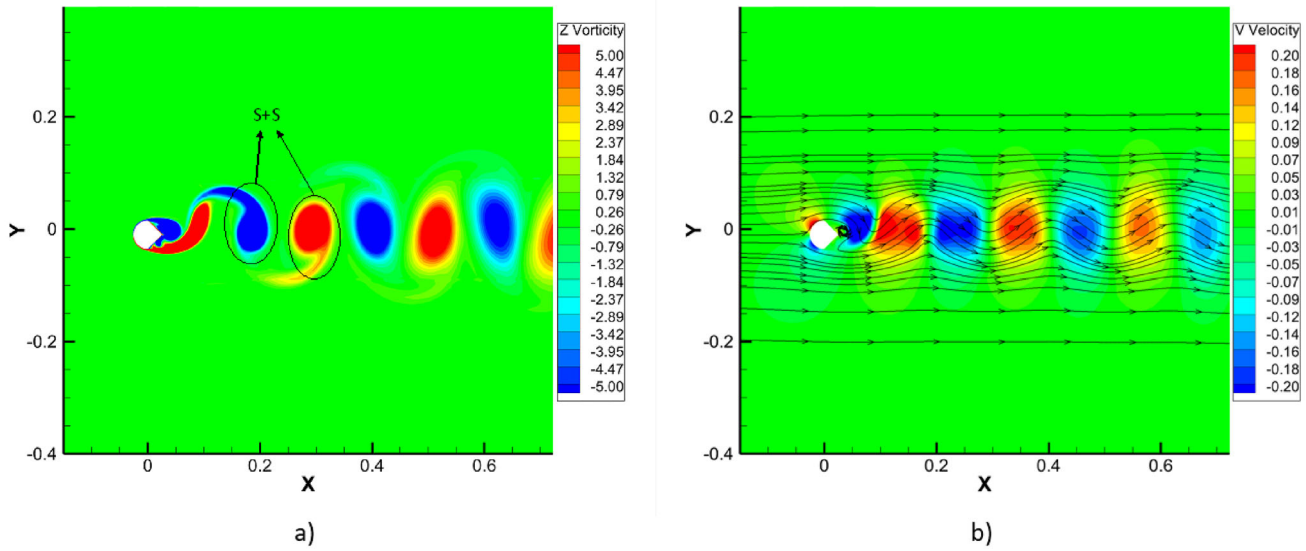

Fig. 25 **a** Vorticity field and **b** streamlines around the Prism with submergence depth ratio $S^* = + +$ at $U^* = 14$ (Re = 12,676)

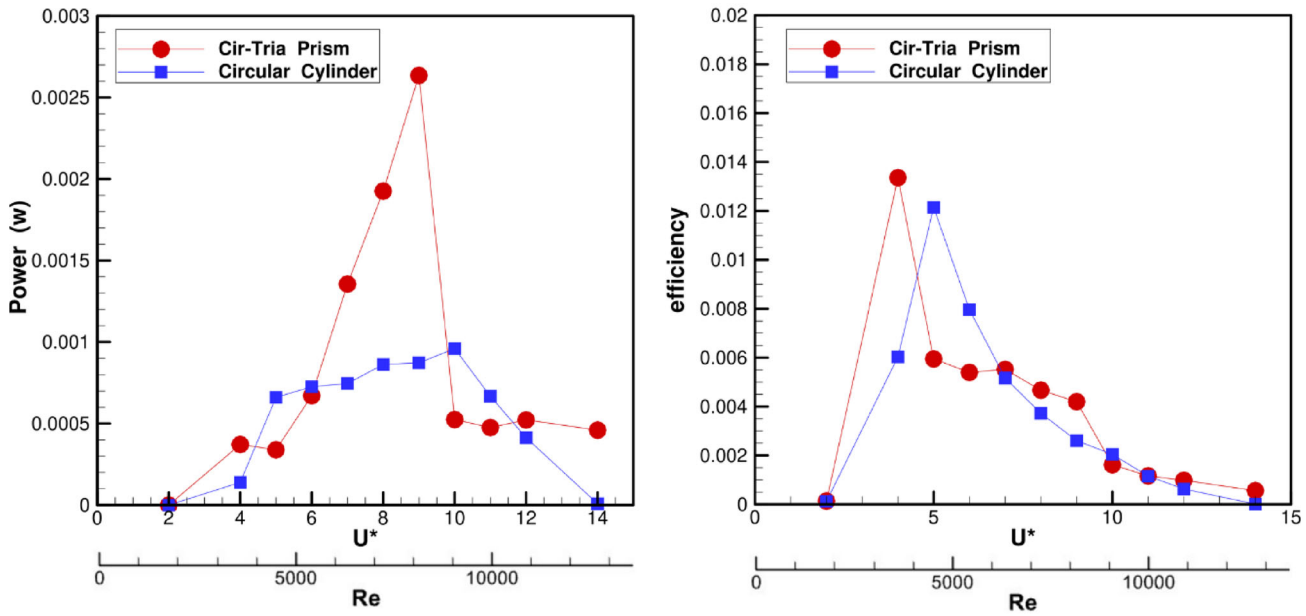

Fig. 26 Converted power and energy conversion efficiency of circular cylinder and cir-tria prism

In summary, the relationship between FIM submergence depth and FIM extracted energy depends on the following factors: Submergence depth factors, Flow velocity and FIM branch. It is possible to obtain the optimal value of reduced velocity and submergence depth among the available modes based on a particular application.

In future research, it will be crucial to investigate the actual velocity profiles in shallow water environments to better reflect real-world conditions. Additionally, conducting three-dimensional simulations would provide deeper insights into the physical phenomena and governing mechanisms at play. These improvements would help enhance the accuracy of the models and contribute to a more comprehensive understanding of FIM, leading to more effective applications in energy-harvesting and other related field.

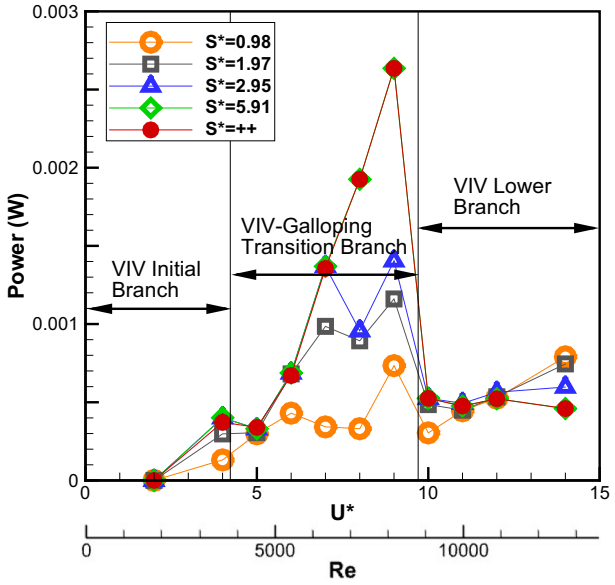

Fig. 27 Converted power of the Cir-Tria Prism for different submergence depth ratios

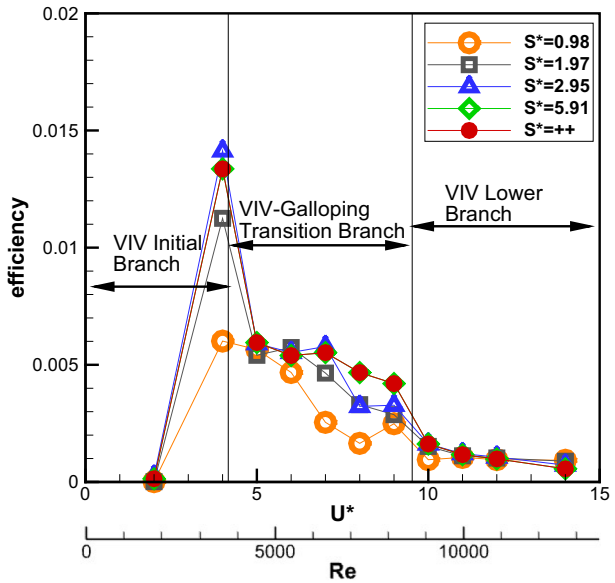

Fig. 28 Energy conversion efficiency of the Cir-Tria Prism for different submergence depth ratios

Author contributions M.M. (Mehran Masdari) led the research, created the idea, funded the project, wrote the initial manuscript, and reviewed the entire paper. A.S. (Ali Sharifi) wrote the main body of the text and performed the simulations. M.O. (Mohammad Omidyeganeh) reviewed and provided advice on the manuscript. All authors reviewed and approved the final manuscript.

Data availability No datasets were generated or analyzed during the current study.

Declarations

Conflict of interest The authors declare no competing interests.

References

Babaie Z, Moslem F, Masdari M, Tahani M (2022) Numerical investigation on VIV energy harvesting enhancement with adding eccentricity to a circular cylinder. Int J Thermofluid Sci Technol 9(5):502–523. https://doi.org/10.36963/IJTST.2022090502

Bernitsas MM (2016) Harvesting energy by flow-induced motions. In: Dhanak MR, Xiros NI (eds) Springer handbook of ocean engineering. Springer, pp 1163–1244

Bernitsas MM, Raghavan K, Ben-Simon Y, Garcia E (2006) VIVACE (Vortex Induced Vibration Aquatic Clean Energy): A new concept in generation of clean and renewable energy from fluid flow. In Proceedings of the International Conference on Offshore Mechanics and Arctic Engineering (OMAE2006), Hamburg, Germany.

Bernitsas M, Raghavan K, Maroulis D (2007) Effect of free surface on VIV for energy harnessing at 8× 103< Re< 1.5× 105. In: Proceedings of the 26th International Conference on Offshore Mechanics and Arctic Engineering (OMAE2007), Paper #29726, San Diego, California.

Bernitsas MM, Raghavan K, Ben-Simon Y, Garcia EMH (2008) VIVACE (Vortex Induced Vibration Aquatic Clean Energy): A new concept in generation of clean and renewable energy from fluid flow. J Offshore Mech Arctic Engg 130(4):041101-1–041101-15. https://doi.org/10.1115/1.2957913

Carberry J, Sheridan J, Rockwell D (2004) Cylinder oscillations beneath a free-surface. Eur J Mech B Fluids 23(1):81–88. https://doi.org/10.1016/j.euromechflu.2003.08.006

Ding L, Zhang L, Wu C, Mao X, Jiang D (2015) Flow induced motion and energy harvesting of bluff bodies with different cross sections. Energy Convers Manag 91:416–426. https://doi.org/10.1016/j.enconman.2014.12.039

Ding L, Zhang L, Bernitsas MM, Chang C-C (2016) Numerical simulation and experimental validation for energy harvesting of single-cylinder VIVACE converter with passive turbulence control. Renew Energy 85:1246–1259. https://doi.org/10.1016/j.renene.2015.07.077

Gu M, Song B, Zhang B, Mao Z, Tian W (2020) The effects of submergence depth on Vortex-Induced Vibration (VIV) and energy harvesting of a circular cylinder. Renewable Energy 151:931–945. https://doi.org/10.1016/j.renene.2019.11.086

Guilmineau E, Queutey P (2004) Numerical simulation of vortex-induced vibration of a circular cylinder with low mass-damping in a turbulent flow. J Fluids Struct 19(4):449–466. https://doi.org/10.1016/j.jfluidstructs.2004.02.004

Hirt CW, Nichols BD (1981) Volume of fluid (VOF) method for the dynamics of free boundaries. J Comput Phys 39(1):201–225. https://doi.org/10.1016/0021-9991(81)90145-5

Jauvtis N, Williamson CHK (2004) The effect of two degrees of freedom on vortex-induced vibration at low mass and damping. J Fluid Mech 509:23–62. https://doi.org/10.1017/S0022112004008778

Jebelli M, Masdari M (2022a) Interaction of free oscillating flat plate and VIV of a circular cylinder in laminar flow. J Fluids Struct 113:103648. https://doi.org/10.1016/j.jfluidstructs.2022.103648

Jebelli M, Masdari M (2022b) Interaction of two parallel free oscillating flat plates and VIV of an upstream circular cylinder in laminar flow. Ocean Eng 259:111876. https://doi.org/10.1016/j.oceaneng.2022.111876

Khalak A, Williamson CHK (1996) Dynamics of a hydroelastic cylinder with very low mass and damping. J Fluids Struct 10(5):455–472. https://doi.org/10.1006/jfls.1996.0031

Khalak A, Williamson CHK (1999) Motions, forces and mode transitions in vortex-induced vibrations at low mass-damping. J Fluids Struct 13(7–8):813–851. https://doi.org/10.1006/jfls.1999.0236

Kim ES, Bernitsas MM (2016) Performance prediction of horizontal hydrokinetic energy converter using multiple-cylinder synergy in flow induced motion. Appl Energy 170:92–100. https://doi.org/10.1016/j.apenergy.2016.02.116

Lee JH, Xiros NI, Bernitsas MM (2011) Virtual damper–spring system for VIV experiments and hydrokinetic energy conversion. Ocean Eng 38(5–6):732–747. https://doi.org/10.1016/j.oceaneng.2010.12.014

Mao Z, Zhao F (2017) Structure optimization of a vibration suppression device for underwater moored platforms using CFD and neural network. Complexity. https://doi.org/10.1155/2017/5392539

Newmark NM (1959) A method of computation for structural dynamics. J Eng Mech Div 85(3):67–94. https://doi.org/10.1061/JMCEA3.0000098

Oliveira PJ, Issa RI (2001) An improved PISO algorithm for the computation of buoyancy-driven flows. Numer Heat Transfer Part B Fund 40(6):473–493. https://doi.org/10.1080/104077901753306601

Park H, Kumar RA, Bernitsas MM (2013) Enhancement of flow-induced motion of rigid circular cylinder on springs by localized surface roughness at $3\times10^4 \leq \mathrm{Re} \leq 1.2\times10^5$. Ocean Eng 72:403–415. https://doi.org/10.1016/j.oceaneng.2013.06.026

Raghavan K (2007) Energy extraction from a steady flow using vortex induced vibration (Doctoral dissertation, University of Michigan, USA). Retrieved from https://hdl.handle.net/2027.42/55687

Reichl P, Hourigan K, Thompson MC (2005) Flow past a cylinder close to a free surface. J Fluid Mech 533:269–296. https://doi.org/10.1017/S0022112005004209

Rostami AB, Armandei M (2017) Renewable energy harvesting by vortex-induced motions: Review and benchmarking of technologies. Renew Sustain Energy Rev 70:193–214. https://doi.org/10.1016/j.rser.2016.11.202

Sun H, Ma C, Kim ES, Nowakowski G, Mauer E, Bernitsas MM (2017) Hydrokinetic energy conversion by two rough tandem-cylinders in flow induced motions: Effect of spacing and stiffness. Renewable Energy 107:61–80. https://doi.org/10.1016/j.renene.2017.01.043

Williamson CHK, Jauvtis N (2004) A high-amplitude 2T mode of vortex-induced vibration for a light body in XY motion. Eur J Mech B Fluids 23(1):107–114. https://doi.org/10.1016/j.euromechflu.2003.09.008

Williamson CHK, Roshko A (1988) Vortex formation in the wake of an oscillating cylinder. J Fluids Struct 2(4):355–381. https://doi.org/10.1016/S0889-9746(88)90058-8

Zdravkovich MM (2003) Flow around circular cylinders: a comprehensive guide through flow phenomena, experiments, applications, mathematical models, and computer simulations. Oxford University Press, Oxford, pp 1997–2003

Zhang B, Song B, Mao Z, Tian W, Li B (2017) Numerical investigation on VIV energy harvesting of bluff bodies with different cross sections in tandem arrangement. Energy 133:723–736. https://doi.org/10.1016/j.energy.2017.05.051

Zhang B, Wang K-H, Song B, Mao Z, Tian W (2018) Numerical investigation on the effect of the cross-sectional aspect ratio of a rectangular cylinder in FIM on hydrokinetic energy conversion. Energy 165:949–964. https://doi.org/10.1016/j.energy.2018.09.138

Zhao M, Cheng L, Zhou T (2013) Numerical simulation of vortex-induced vibration of a square cylinder at a low Reynolds number. Phys Fluids 25(2):023603. https://doi.org/10.1063/1.4792351

Zhao M, Cheng L, An H, Tong F (2015) Flow and flow-induced vibration of a square array of cylinders in steady currents. Fluid Dyn Res 47(4):045505. https://doi.org/10.1088/0169-5983/47/4/045505

Zhu Q, Lin J-C, Unal M, Rockwell D (2000) Motion of a cylinder adjacent to a free-surface: flow patterns and loading. Exp Fluids 28(6):559–575. https://doi.org/10.1007/s003480050416